Received October 13, 2014; accepted December 10, 2014
Preprint typeset using LaTeX style emulateapj v. 5/2/11

arXiv:1412.3899v1 [astro-ph.GA] 12 Dec 2014

GROUND-BASED PAα NARROW-BAND IMAGING OF LOCAL LUMINOUS INFRARED GALAXIES I: STAR FORMATION RATES AND SURFACE DENSITIES

Ken Tateuchi[1], Masahiro Konishi[1], Kentaro Motohara[1], Hidenori Takahashi[1], Natsuko Mitani Kato[1], Yutaro Kitagawa[1], Soya Todo[1], Koji Toshikawa[1], Shigeyuki Sako[1], Yuka K. Uchimoto[1,3], Ryou Ohsawa[1], Kentaro Asano[1], Yoshifusa Ita[3], Takafumi Kamizuka[1], Shinya Komugi[4], Shintaro Koshida[5], Sho Manabe[7], Tomohiko Nakamura[1,2], Asami Nakashima[2,6], Kazushi Okada[1], Toshinobu Takagi[8], Toshihiko Tanabé[1], Mizuho Uchiyama[1], Tsutomu Aoki[9], Mamoru Doi[1,10], Toshihiro Handa[11], Kimiaki Kawara[1], Kotaro Kohno[1,10], Takeo Minezaki[1], Takashi Miyata[1], Tomoki Morokuma[1], Takeo Soyano[9], Yoichi Tamura[1], Masuo Tanaka[1], Ken'ichi Tarusawa[9], Yuzuru Yoshii[1]

[1] Institute of Astronomy, Graduate School of Science, The University of Tokyo, 2-21-1 Osawa, Mitaka, Tokyo 181-0015, Japan
[2] Department of Astronomy, Graduate School of Science, The University of Tokyo, 7-3-1 Hongo, Bunkyo-ku, Tokyo 113-0033, Japan
[3] Astronomical Institute, Tohoku University, 6-3 Aoba, Aramaki, Aoba-ku, Sendai, Miyagi 980-8578, Japan
[4] Division of Liberal Arts, Kogakuin University, 2665-1, Hachioji, Tokyo 192-0015, Japan
[5] Subaru Telescope, National Astronomical Observatory of Japan, Hilo, HI 96720, USA
[6] National Astronomical Observatory, Mitaka, Tokyo 181-8588, Japan
[7] Department of Earth and Planetary Sciences, Kobe University, 657-8501 Kobe, Japan
[8] Institute of Space and Astronautical Science, Japan Aerospace Exploration Agency, 3-1-1 Yoshinodai, Sagamihara, Kanagawa 229-8510, Japan
[9] Kiso Observatory, Institute of Astronomy, The University of Tokyo, 10762-30, Mitake, Kiso-machi, Kiso-gun, Nagano 397-0101, Japan
[10] Research Center for the Early Universe (RESCEU), University of Tokyo, 7-3-1, Hongo, Bunkyo, Tokyo 113-0033, Japan and
[11] Faculty of Science, Kagoshima University, Korimoto 1-21-24, Kagoshima 890-8580, Japan

Received October 13, 2014; accepted December 10, 2014

ABSTRACT

Luminous infrared galaxies (LIRGs) are enshrouded by a large amount of dust, produced by their active star formation, and it is difficult to measure their activity in the optical wavelength. We have carried out Paα narrow-band imaging observations of 38 nearby star-forming galaxies including 33 LIRGs listed in *IRAS* RBGS catalog with the Atacama Near InfraRed camera (ANIR) on the University of Tokyo Atacama Observatory (TAO) 1.0 m telescope (miniTAO). Star formation rates (SFRs) estimated from the Paα fluxes, corrected for dust extinction using the Balmer Decrement Method (typically $A_V \sim 4.3$ mag), show a good correlation with those from the bolometric infrared luminosity of *IRAS* data within a scatter of 0.27 dex. This suggests that the correction of dust extinction for Paα flux is sufficient in our sample. We measure the physical sizes and the surface density of infrared luminosities ($\Sigma_{L(\mathrm{IR})}$) and SFR (Σ_{SFR}) of star-forming region for individual galaxies, and find that most of the galaxies follow a sequence of local ultra luminous or luminous infrared galaxies (U/LIRGs) on the L(IR)-$\Sigma_{L(\mathrm{IR})}$ and SFR-Σ_{SFR} plane. We confirm that a transition of the sequence from normal galaxies to U/LIRGs is seen at $L(\mathrm{IR}) = 8 \times 10^{10}\ L_\odot$. Also, we find that there is a large scatter in physical size, different from those of normal galaxies or ULIRGs. Considering the fact that most of U/LIRGs are merging or interacting galaxies, this scatter may be caused by strong external factors or differences of their merging stage.

Subject headings: galaxies:interactions — galaxies:starburst — HII regions — stars:formation — infrared: galaxies

1. INTRODUCTION

In recent years, many large deep cosmological surveys have been performed in various wavelengths, including ultraviolet, visible, infrared and submillimeter. These surveys have revealed that the star formation rate (SFR) density of the universe (cosmic SFR density, cSFRD) increases with redshift, and peaks at $1 < z < 3$ (e.g., Rujopakarn et al. 2010; Hopkins & Beacom 2006). It is known that the cSFRD at the high-redshift universe is dominated by bright infrared galaxies; ULIRGs (Ultra Luminous Infrared Galaxies; $L(\mathrm{IR}) \equiv L$ (8–1000 μm) $\geq 10^{12}\ L_\odot$) and LIRGs (Luminous Infrared Galaxies; $L(\mathrm{IR}) \equiv 10^{11}$–$10^{12}\ L_\odot$) dominate 80% of total star formation activities at $z \sim 1$ (e.g., Caputi et al. 2007; Goto et al. 2010), and these galaxies are in the starburst sequence which have high star formation efficiency (SFE = SFR ($M_\odot$ yr^{-1})/M_{gas} ($M_\odot$)) of around 10^{-8} yr^{-1} (e.g., Lada et al. 2012; Daddi et al. 2010) in contrast of 10^{-9} yr^{-1} for normal galaxies. In order to probe the detailed properties of these galaxies, and to understand how they have been formed and evolved, nearby ULIRGs and LIRGs are ideal laboratories because they can be spatially resolved.

In the local universe, normal galaxies show extended star-forming regions over a few kilo-parsecs along the spiral arms, while distributions of star-forming regions of LIRGs at the high infrared luminosity end ($\log(L(\mathrm{IR})/L_\odot) = 11.8$–$12.0$) and ULIRGs, which are considered to be in the starburst sequence, become very compact and concentrated at central regions (e.g., Soifer et al. 2000; Díaz-Santos et al. 2010; Rujopakarn et al. 2011 (R11); Alonso-Herrero et al. 2012). However, the relationship between star formation activities and spatial

distribution of star-forming regions, and the mechanism of starburst is still an open question. Some simulations of galaxy formation suggest that the central concentration of stars and gases is formed by interacting/merging systems, which accumulates dense gas clouds and triggers starburst (Barnes & Hernquist 1996). However, there have been not enough observational studies to reveal the relations.

To understand the detailed mechanism of starburst activities in U/LIRGs, the star formation rate is one of the most important parameters. Many indicators for estimation of star formation rate, such as X-ray, ultraviolet (UV), Hα, mid-infrared (MIR), and far-infrared (FIR) emission have been used. Hydrogen recombination lines, which is emitted from the current star-forming regions within 10 Myr (Sanders & Mirabel 1996), are direct tracers of star-forming region. Especially, optical hydrogen recombination lines such as Hα and Hβ are usually used because they can be observed easily. However, U/LIRGs are affected by a large amount of dust (extinction of $A_V \sim 3$ mag for LIRGs; Alonso-Herrero et al. 2006, and $A_V > 10$ mag for ULIRGs; Piqueras López et al. 2013), typically associated with the regions of active star formation. Therefore, those lines are easily attenuated by the dust. Wherein the hydrogen Paα emission line (1.8751 μm) is a good tracer of the dusty star-forming region because of its insensitivity to the dust-extinction (Alonso-Herrero et al. 2006) and being the strongest emission line in the near-infrared wavelength range (NIR, $\lambda \sim 0.9$–2.5 μm), which can reach higher spatial resolution easily than in the MIR and FIR. However, because of poor atmospheric transmission around the wavelength of Paα emission line (Figure 1) due to absorptions mainly by water vapor, no Paα imaging from a ground-based telescope is reported so far, although there are some spectroscopic observations of Paα in redshifted galaxies (e.g., Hill et al. 1996; Falcke et al. 1998; Murphy et al. 1999; Kim et al. 2010). To overcome these difficulties, it is necessary to observe the emission line by either a space-borne facilities such as the Near Infrared Camera and Multi-object Spectrometer (NICMOS) on *Hubble Space Telescope* (*HST*) (e.g., Scoville et al. 2001; Alonso-Herrero et al. 2006; Liu et al. 2013a) or facilities built at sites with low PWV. However, some researchers have pointed out that *HST*/NICMOS (already decommissioned in 2010) may be insensitive to diffuse Paschen-alpha emission due to its intrinsic high angular resolution (e.g., Alonso-Herrero et al. 2006; Calzetti et al. 2007; Kennicutt et al. 2007; Rieke et al. 2009).

Therefore, we have been carrying out Paα narrow-band imaging observations (Tateuchi et al. 2012a, 2013) with Atacama Near InfraRed camera (ANIR; Motohara et al. 2008, Konishi et al. 2014; K14), on the University of Tokyo Atacama Observatory (TAO, Yoshii et al. 2010) 1.0m telescope (miniTAO; Minezaki et al. 2010) installed at the summit of Co. Chajnantor (5640m altitude) in northern Chile to understand distributions of star-forming region and properties of dust-enshrouded infrared galaxies in the local universe. Thanks to the high altitude and the extremely low water vapor content of the site we can stably observe Paα emission line has been observationally confirmed (Motohara et al. 2010, 2011; Tanabé et al. 2013).

In this paper, we describe our sample of luminous infrared galaxies and the observation procedure in § 2, the method of data reduction and flux calibration in § 3, and the derived Paα flux and properties of individual galaxies in § 4. In § 5, we evaluate the selection bias due to our luminosity-limited sample, the effects of dust-extinction, the relationship between SFRs estimated from Paα and those from FIR fluxes, and the properties of surface densities of SFR. Then, we summarize them in § 6.

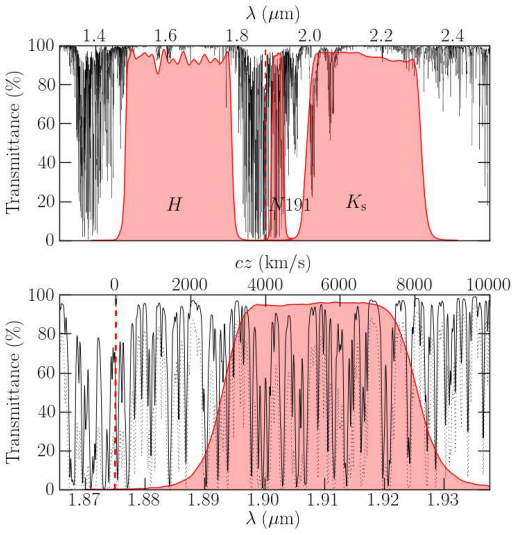

FIG. 1.— Top: atmospheric transmittance in the wavelength range containing the H- and the K_s-band. The bold line represents the difference of the median value of the transmittance at the TAO site (altitude of 5,640 m, PWV = 0.5 mm) and that at the VLT site (2,600 m, PWV = 2.0 mm), both calculated by ATRAN (Lord 1992). The shaded area with red shows the filter transmittance curve of the H-band, $N191$, and K_s-band filters. Bottom: atmospheric transmittance around the $N191$ filter. The bold line corresponds to that at the TAO site, and the dotted line at the VLT site. The overlaid thick red area shows the transmittance of the $N191$ filter. The dashed vertical red line in the both plots represents the wavelength of the rest-frame Paα (1.8751 μm).

Throughout this paper, we use a Λ-CDM cosmology with $\Omega_m = 0.3$, $\Omega_\Lambda = 0.7$, and $H_0 = 70$ km s^{-1} Mpc^{-1}.

2. OBSERVATIONS

2.1. *The Sample*

We have selected the target galaxies from the *IRAS* Revised Bright Galaxy Sample (RBGS : Sanders et al. 2003). The location of the observatory limits the declination of the targets to be $< 30°$. The wavelength range of the $N191$ narrow-band filter limits the recession velocity to be 2800 km s^{-1} – 8100 km s^{-1}, corresponding to the distances of 46.6 Mpc – 109.6 Mpc. From these conditions, the number of observable galaxies in the RBGS is 151, and we have observed 38 galaxies out of them at random. The selected galaxies are listed in Table 1. In our sample, the bolometric infrared luminosity (L(IR)) ranges between 4.5×10^{10} $L_\odot$ and 6.5×10^{11} $L_\odot$, which ranges from the high luminosity end of normal galaxies to LIRGs.

2.2. *Observation with Atacama Near Infrared Camera*

The observations have been carried out using Atacama NIR camera (ANIR; Motohara et al. 2008, K14) installed

TABLE 1
Sample of Local Luminous Infrared Galaxies

ID (1)	Galaxy Name (2)	IRAS Name (3)	R.A. (J2000) (4)	Dec. (J2000) (5)	cz (km s^{-1}) (6)	Dist. (Mpc) (7)	log$L_{\rm IR}$ ($L_\odot$) (8)	Spectral Class (9)	Obs. Date (10)
1	NGC 23	F00073+2538	00 09 55.1	+25 55 37	4536	65.6	11.13	HII	2009-10-26
2	NGC 34	F00085−1223	00 11 06.6	−12 06 27	5931	86.0	11.52	Sy2	2011-10-22
3	NGC 232	F00402−2349	00 42 46.5	−23 33 31	6047	87.7	11.39	HII	2009-10-21
4	IC 1623A/B	F01053−1746	01 07 46.3	−17 30 32	6028	87.4	11.74	HII	2009-10-17
5	ESO 244-G012	F01159−4443	01 18 08.6	−44 27 40	6866	99.8	11.48	LINER	2009-10-21
6	UGC 2238	F02435+1253	02 46 17.0	+13 05 45	6436	93.5	11.33	LINER	2009-10-27
7	IRAS F02437+2122	F02437+2122	02 46 38.3	+21 35 06	6987	101.6	11.21	LINER	2009-10-22
8	UGC 2982	F04097+0525	04 12 22.4	+05 32 49	5161	74.7	11.20	HII	2011-10-19
9	NGC 1614	F04315−0840	04 34 00.1	−08 34 46	4746	68.6	11.66	HII/Sy2	2009-10-15
10	MCG −05-12-006	F04502−3304	04 52 06.8	−32 59 24	5622	81.5	11.17	HII	2009-10-14
11	NGC 1720	F04569−0756	04 59 19.9	−07 51 34	4186	60.4	10.90	N	2011-10-19
12	ESO 557-G002	F06295−1735	06 31 46.3	−17 37 15	6339	92.0	11.24	HII	2009-10-19
13	IRAS F06592-6313	F06592−6313	06 59 40.3	−63 17 53	6882	100.0	11.20	HII	2009-10-27
14	NGC 2342	07063+2043	07 09 19.6	+20 38 12	5276	76.4	11.40	HII	2009-10-23
15	ESO 320-G030	F11506−3851	11 53 12.0	−39 07 54	3232	46.6	11.28	HII	2011-04-21
16	NGC 4922	F12590+2934	13 01 25.9	+29 18 46	7071	102.8	11.33	LINER	2009-06-13
17	MCG −03-34-064	F13197−1627	13 22 23.5	−16 43 34	5152	74.6	11.28	Sy1	2011-04-28
18	NGC 5135	F13229−2934	13 25 43.0	−29 49 54	4114	59.4	11.27	Sy2	2011-04-28
19	NGC 5257/8	F13373+0105	13 39 54.9	+00 50 07	6798	98.8	11.54	HII	2011-04-27
20	IC 4518A/B	F14544−4255	14 57 43.1	−43 08 01	4715	68.2	11.09	Sy2	2011-04-24
21	IC 4687/86	F18093−5744	18 13 38.6	−57 43 36	5188	75.0	11.55	HII (both)	2011-04-25
22	IRAS F18293-3413	F18293−3413	18 32 40.2	−34 11 26	5449	78.9	11.82	HII	2009-06-12
23	ESO 339-G011	F19542−3804	19 57 37.5	−37 56 10	5722	82.9	11.14	Sy2	2009-10-25
24	NGC 6926	F20304−0211	20 33 04.8	−02 01 39	5970	86.6	11.32	Sy2	2009-06-12
25	IC 5063	F20482−5715	20 52 03.5	−57 04 03	3380	48.7	10.86	Sy2	2010-10-15
26	ESO 286-G035	F21008−4347	21 04 11.2	−43 35 34	5208	75.4	11.25	HII	2009-10-27
27	ESO 343-IG013	F21330−3846	21 36 10.8	−38 32 38	5714	82.8	11.10	HII	2009-10-25
28	NGC 7130	F21453−3511	21 48 19.6	−34 57 05	4824	69.8	11.39	LINER/Sy1	2009-10-26
29	IC 5179	F22132−3705	22 16 10.0	−36 50 35	3398	49.0	11.21	HII	2010-10-14
30	ESO 534-G009	F22359−2606	22 38 40.8	−25 51 05	3393	48.9	10.70	LINER	2010-10-07
31	NGC 7469	F23007+0836	23 03 15.5	+08 52 25	4922	71.2	11.67	Sy1	2009-10-22
32	CGCG 453-062	F23024+1916	23 04 55.2	+19 33 01	7524	109.6	11.41	LINER	2010-10-19
33	NGC 7591	F23157+0618	23 18 15.7	+06 35 06	4961	71.8	11.11	LINER	2011-10-16
34	NGC 7678	F23259+2208	23 28 27.0	+22 25 09	3482	50.2	10.84	HII	2010-10-20
35	MCG −01-60-022	F23394−0353	23 42 02.2	−03 36 48	6966	101.3	11.29	HII	2009-10-17
36	NGC 7771	F23488+1949	23 51 24.7	+20 06 39	4336	62.6	11.42	HII	2009-10-27
37	Mrk 0331	F23488+2018	23 51 26.1	+20 35 08	5371	77.8	11.48	HII/Sy2	2010-10-15
38	UGC 12914/15	F23591+2312	00 01 40.7	+23 29 37	4534	65.5	10.99	LINER	2010-10-09

Note. — Column (1): Galaxy ID in this paper. Column (2): Galaxy name. Column (3): IRA catalog ID. Column (4): Right Ascension for the epoch 2000. Column (5): Declination for the epoch 2000. Column (6): Recession velocity. Column (7): Luminosity distance based on the parameters of Λ-CDM cosmology (e.g., Spergel et al. 2003). Column (8): Bolometric Infrared luminosities ($L_{\rm IR(8-1000\mu m)}$ ($L_\odot$)) in Sanders et al. (2003) corrected for the different cosmic parameters. Column (9): Classification by optical spectroscopic observation taken from Kim et al. (1998) and Alonso-Herrero et al. (2006). Sy1: Seyfert 1, Sy2: Seyfert 2, LINER: LINER, HII: HII region. (10): Observation date, yyyy-mm-dd.

at the Cassegrain focus of the University of Tokyo Atacama Observatory (TAO, Yoshii et al. 2010) 1.0 m telescope (miniTAO; Minezaki et al. 2010).The observatory is located at the summit of Co. Chajnantor (5640m altitude) in northern Chile.

The value of the precipitable water vapor (PWV) is 0.1–0.7 mm (K14), and the atmospheric window opens around the wavelength of Paα (1.8751 μm). The median value of the PWV during the observation is 0.5 mm which is described in section 3.2. Figure 1 shows the simulated atmospheric transmittance with the ATRAN (Lord 1992) at the TAO site. It can be seen that the TAO site (altitude of 5,640 m, bold line) shows higher transmission than the Very Large Telescope (VLT) site at a lower altitude (2,600 m, dotted line), especially at the wavelength range around Paα.

We have carried out 5 observation runs from 2009 to 2011. 38 targets (44 individual galaxies) have been observed with the $N191$ narrow-band filter, which has the central wavelength ($\lambda_{\rm c}$) of 1.9105 μm with a FWHM of 0.0079 μm ($\Delta\lambda$) to cover redshifted Paα line. Also, we have carried out the observations with the H and $K_{\rm s}$ broad-band filters to obtain stellar continuum images. The profiles of these filters are also shown in Figure 1. Typical seeing size is 0.″8 during the observations. The total integration time for each galaxy is 540 s (60 s × 9 dithering) for the H and $K_{\rm s}$ filters, and 1620 s (180 s × 9 dithering) for the $N191$ except for UGC 12914/5 which is observed with longer integration time of 12420 s for a detailed study (Komugi et al. 2012). As the Paα emission line is strongly affected by the PWV, the observations have been carried out during nights with low PWV (about 0.5 mm; details are described in the next section).

3. DATA REDUCTIONS

3.1. *Reduction Procedure*

The data are reduced using the standard IRAF software packages. In the first step of the data reduction, flat pattern and sky background are removed from raw images. A flat pattern image is made from a sky image produced by stacking all object-masked images per

TABLE 2
Paα fluxes and derived quantities of atmospheric condition with miniTAO/ANIR.

ID (1)	Galaxy Name (2)	$f(\mathrm{Pa}\alpha)$ (ergs cm^{-2} s^{-1}) (3)	$\sigma(\mathrm{Pa}\alpha)_{\mathrm{phot}}$ (ergs cm^{-2} s^{-1}) (4)	$\sigma(\mathrm{Pa}\alpha)_{\mathrm{atm}}$ (ergs cm^{-2} s^{-1}) (5)	$f(\mathrm{Pa}\alpha)_{\mathrm{miss}}$ (ergs cm^{-2} s^{-1}) (6)	PWV (μm) (7)	$(T_{\mathrm{atm}}^{\mathrm{PWV},N191})^X$ (%) (8)	T_{line} (%) (9)
1	NGC 23	2.28×10^{-13}	$\pm 7.21\times10^{-16}$	$\pm 2.79\times10^{-14}$	$+ 4.33\times10^{-15}$	629.6	57.3	51.4
2	NGC 34	3.73×10^{-13}	$\pm 1.54\times10^{-15}$	$\pm 4.55\times10^{-14}$	$+ 1.05\times10^{-14}$	485.7	63.2	55.6
3	NGC 232	8.66×10^{-14}	$\pm 9.29\times10^{-16}$	$\pm 1.06\times10^{-14}$	$+ 4.84\times10^{-15}$	197.3	74.1	66.3
4	IC 1623A/B	6.58×10^{-13}	$\pm 5.81\times10^{-16}$	$\pm 8.03\times10^{-14}$	$+ 2.62\times10^{-15}$	446.3	64.7	55.4
5	ESO 244-G012	3.63×10^{-13}	$\pm 6.88\times10^{-16}$	$\pm 4.43\times10^{-14}$	$+ 4.66\times10^{-15}$	385.6	67.1	85.6
6	UGC 2238	3.71×10^{-13}	$\pm 1.42\times10^{-15}$	$\pm 4.53\times10^{-14}$	$+ 9.88\times10^{-15}$	576.6	59.2	60.6
7	IRAS F02437±2122	1.99×10^{-14}	$\pm 1.26\times10^{-15}$	$\pm 2.42\times10^{-15}$	$+ 5.35\times10^{-15}$	359.7	68.1	81.4
8	UGC 2982	4.00×10^{-13}	$\pm 7.62\times10^{-16}$	$\pm 4.88\times10^{-14}$	$+ 4.00\times10^{-15}$	82.7	83.4	80.2
9	NGC 1614	1.06×10^{-12}	$\pm 1.18\times10^{-15}$	$\pm 1.29\times10^{-13}$	$+ 8.53\times10^{-15}$	507.5	62.3	50.1
10	MCG −05-12-006	1.61×10^{-13}	$\pm 6.69\times10^{-16}$	$\pm 1.97\times10^{-14}$	$+ 5.44\times10^{-15}$	1035.1	48.1	55.5
11	NGC 1720	7.60×10^{-14}	$\pm 3.21\times10^{-16}$	$\pm 9.28\times10^{-15}$	$+ 2.04\times10^{-15}$	74.9	84.3	82.9
12	ESO 557-G002	8.90×10^{-13}	$\pm 5.56\times10^{-16}$	$\pm 1.09\times10^{-14}$	$+ 2.89\times10^{-15}$	435.0	65.2	61.9
13	IRAS F06592-6313	6.17×10^{-14}	$\pm 6.52\times10^{-16}$	$\pm 7.53\times10^{-15}$	$+ 3.66\times10^{-15}$	701.3	55.1	78.4
14	NGC 2342	2.22×10^{-13}	$\pm 7.66\times10^{-16}$	$\pm 2.71\times10^{-14}$	$+ 4.46\times10^{-15}$	1307.5	43.9	56.1
15	ESO 320-G030	1.64×10^{-13}	$\pm 4.98\times10^{-16}$	$\pm 2.00\times10^{-14}$	$+ 2.24\times10^{-15}$	532.5	61.2	81.9
16	NGC 4922	4.35×10^{-14}	$\pm 7.20\times10^{-16}$	$\pm 5.30\times10^{-15}$	$+ 3.10\times10^{-15}$	516.2	61.9	65.9
17	MCG −03-34-064	1.12×10^{-13}	$\pm 1.41\times10^{-17}$	$\pm 1.37\times10^{-14}$	$+ 3.68\times10^{-16}$	512.2	62.0	57.8
18	NGC 5135	4.09×10^{-13}	$\pm 6.29\times10^{-16}$	$\pm 4.99\times10^{-14}$	$+ 3.28\times10^{-15}$	759.3	53.4	39.0
19a	NGC 5257	2.27×10^{-13}	$\pm 2.28\times10^{-16}$	$\pm 2.76\times10^{-14}$	$+ 1.05\times10^{-15}$	913.5	50.2	70.5
19b	NGC 5258	1.66×10^{-13}	$\pm 2.34\times10^{-16}$	$\pm 2.02\times10^{-14}$	$+ 8.62\times10^{-16}$	913.5	50.2	70.5
20a	IC 4518A	8.11×10^{-14}	$\pm 6.30\times10^{-16}$	$\pm 9.89\times10^{-15}$	$+ 2.73\times10^{-15}$	547.2	60.5	50.6
20b	IC 4518B	5.15×10^{-14}	$\pm 1.06\times10^{-15}$	$\pm 6.28\times10^{-15}$	$+ 3.31\times10^{-15}$	547.2	60.5	50.6
21a	IC 4686	1.31×10^{-13}	$\pm 4.03\times10^{-16}$	$\pm 1.60\times10^{-14}$	$+ 3.02\times10^{-15}$	923.8	50.0	50.9
21b	IC 4687	8.04×10^{-13}	$\pm 3.75\times10^{-16}$	$\pm 9.80\times10^{-14}$	$+ 1.88\times10^{-15}$	923.8	50.0	50.9
21c	IC 4689	2.21×10^{-13}	$\pm 4.96\times10^{-16}$	$\pm 2.57\times10^{-14}$	$+ 5.58\times10^{-15}$	923.8	50.0	50.9
22	IRAS F18293-3413	8.44×10^{-13}	$\pm 7.40\times10^{-16}$	$\pm 1.03\times10^{-13}$	$+ 3.62\times10^{-14}$	621.7	57.5	73.6
23	ESO 339-G011	8.95×10^{-14}	$\pm 8.77\times10^{-16}$	$\pm 1.09\times10^{-14}$	$+ 5.01\times10^{-15}$	596.7	58.3	57.5
24	NGC 6926	1.29×10^{-13}	$\pm 8.28\times10^{-16}$	$\pm 1.57\times10^{-14}$	$+ 4.75\times10^{-15}$	441.3	64.9	57.2
25	IC 5063	9.30×10^{-14}	$\pm 3.67\times10^{-16}$	$\pm 1.13\times10^{-14}$	$+ 2.76\times10^{-15}$	350.5	68.4	86.8
26	ESO 286-G035	2.59×10^{-13}	$\pm 7.44\times10^{-16}$	$\pm 3.16\times10^{-14}$	$+ 3.92\times10^{-15}$	526.5	61.4	64.7
27	ESO 343-IG013	8.64×10^{-14}	$\pm 7.40\times10^{-16}$	$\pm 1.05\times10^{-14}$	$+ 3.91\times10^{-15}$	469.7	63.8	63.8
28	NGC 7130	2.32×10^{-13}	$\pm 1.12\times10^{-15}$	$\pm 2.83\times10^{-14}$	$+ 2.46\times10^{-14}$	491.2	62.9	44.1
29	IC 5179	5.65×10^{-13}	$\pm 2.78\times10^{-16}$	$\pm 6.89\times10^{-14}$	$+ 1.17\times10^{-15}$	501.6	62.5	82.4
30	ESO 534-G009	2.28×10^{-14}	$\pm 8.82\times10^{-16}$	$\pm 2.78\times10^{-15}$	$+ 2.92\times10^{-15}$	255.4	71.5	88.6
31	NGC 7469	6.11×10^{-13}	$\pm 8.18\times10^{-16}$	$\pm 7.45\times10^{-14}$	$+ 4.10\times10^{-15}$	156.7	77.1	58.9
32	CGCG 453-062	8.59×10^{-14}	$\pm 3.44\times10^{-16}$	$\pm 1.05\times10^{-14}$	$+ 1.72\times10^{-15}$	172.5	76.0	85.4
33	NGC 7591	1.10×10^{-13}	$\pm 6.39\times10^{-16}$	$\pm 1.34\times10^{-14}$	$+ 3.05\times10^{-15}$	37.4	90.4	81.4
34	NGC 7678	1.13×10^{-13}	$\pm 1.08\times10^{-14}$	$\pm 2.38\times10^{-14}$	$+ 1.92\times10^{-15}$	301.2	70.2	83.0
35	MCG −01-60-022	1.31×10^{-13}	$\pm 6.08\times10^{-16}$	$\pm 1.60\times10^{-14}$	$+ 3.05\times10^{-15}$	328.9	69.2	83.8
36a	NGC 7770	1.87×10^{-13}	$\pm 8.16\times10^{-16}$	$\pm 2.28\times10^{-14}$	$+ 4.21\times10^{-15}$	674.1	55.9	53.5
36b	NGC 7771	3.78×10^{-13}	$\pm 1.78\times10^{-15}$	$\pm 4.61\times10^{-14}$	$+ 9.24\times10^{-15}$	674.1	55.9	53.5
37	MrK 331	2.96×10^{-13}	$\pm 1.06\times10^{-15}$	$\pm 3.60\times10^{-14}$	$+ 5.62\times10^{-15}$	377.1	67.4	81.2
38a	UGC 12914	1.23×10^{-13}	$\pm 2.58\times10^{-16}$	$\pm 1.51\times10^{-14}$	$+ 1.41\times10^{-15}$	364.9	67.9	62.8
38b	UGC 12915	7.49×10^{-14}	$\pm 1.72\times10^{-15}$	$\pm 9.14\times10^{-15}$	$+ 1.07\times10^{-15}$	364.9	67.9	62.8

Note. — Column (1): Galaxy ID in this paper. Column (2): Galaxy name. Column (3): Observed Paα total flux corrected for atmospheric absorption. Column (4): 1σ photometric error of Paα flux. Column (5): Estimated error by the atmospheric absorption correction of the Paα flux. Column (6): 5σ error by continuum subtraction of the Paα flux. Column (7): Estimated PWV using the calibration method described in K14, submitted. Column (8): Estimated effective atmospheric transmittance within the $N191$ filter. Column (9): Estimated the effective line transmittance.

observation run for each filter. The skybackground is removed using a self-sky image which is made by stacking object-masked images in the same dither sequence. We do not correct the image distortions because it is negligible on ANIR. Each image is matched with World Coordinate System (WCS) using position of 2MASS stars (Skrutskie et al. 2006). Then, these images are shifted according to WCS and co-added. In the second step, the flux scale of the combined image is calibrated by 2MASS stars. Comparing stars in the image with those in the 2MASS catalog, zero-point magnitude and system efficiency are derived. Because reference magnitudes of the $N191$ filter are not available we derived them by interpolating the H- and K_{s}- band magnitudes in the 2MASS catalog. Details of this flux calibration procedure are described in K14, arguing that the interpolating calibration technique produces negligible (< 0.01 mag) systematic error. The final H, K_{s} and $N191$ images are convolved with a Gaussian function to match the Point Spread Function (PSF) to the worst among the images (typical spatial resolution of the convolved images is $0\farcs9$). Then, a continuum image is made by interpolating between H and K_{s} images, and we derive a Paα line image by subtracting the continuum image from the $N191$ image.

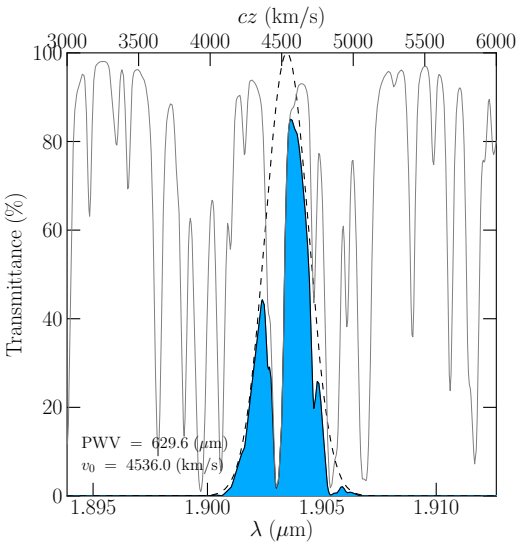

FIG. 2.— An example of Paα emission line we assume a redshifted Paα emission line of NGC 0023, convolved with atmospheric transmittance curve, are shown with the thick solid line. The solid-thin line represents the atmospheric transmittance at PWV = 629.6 (μm) calculated by ATRAN. The dashed line represents an intrinsic Paα line profile without atmospheric absorption. The recession velocity v_0 is set to be 4536 (km s^{-1}), and σ of the intrinsic profile is assumed to be 150 (km s^{-1}).

3.2. *Paα Flux Calibration*

As there are many atmospheric absorption features within the wavelength range of the $N191$ filter whose strength vary temporally with the PWV, it is difficult to calibrate the emission-line flux accurately (Figure 1). To recover the intrinsic Paα fluxes accurately, we have used the following relation:

$$F^{l}_{\rm int} = \frac{(T^{\rm PWV,N191}_{\rm atm})^X}{T_{\rm line}}(f^{N191}_{\rm cal} - f^{H-K_{\rm s}}_{\rm cal})\Delta\lambda, \qquad (1)$$

where $F^{l}_{\rm int}$ is intrinsic Paα flux, $T^{\rm PWV,N191}_{\rm atm}$ is averaged atmospheric transmittance within the wavelength of $N191$ filter toward the zenith (airmass = 1), X is airmass, $T_{\rm line}$ is effective atmospheric transmittance at the wavelength of redshifted Paα emission line, $f^{N191}_{\rm cal}$ is observed flux-calibrated flux of the $N191$ filter, $f^{H-K_{\rm s}}_{\rm cal}$ is continuum flux obtained by interpolating H and $K_{\rm s}$ broad-band images, and $\Delta\lambda$ is FWHM of the $N191$ narrow-band filter. Detailed derivation of Equation (1) is described in Appendix. To obtain the Paα flux, we have to estimate $(T^{\rm PWV,N191}_{\rm atm})^X$ and $T_{\rm line}$.

The factor $(T^{\rm PWV,N191}_{\rm atm})^X$ is obtained using the system efficiency of the H, $N191$ and $K_{\rm s}$ image (K14; Tateuchi et al. 2012b). Then, a PWV is derived from ATRAN model and $(T^{\rm PWV,N191}_{\rm atm})^X$. The factor $T_{\rm line}$ is estimated from a model transmittance curve assuming the Paα emission line profile with the PWV obtained above (details of the estimation is discussed in K14). In a real galaxy, width of an emission line is broadened by more than $\sigma = 100$ km s^{-1} due to velocity dispersion of their emission line clouds. To incorporate this effect, we assume the shape of the emission line to be a Gaussian profile with $\sigma = 150$ km s^{-1} for all the galaxies (Figure 2), which shows the least difference between the Paα fluxes obtained by the above method and those from narrow-band images by HST/NICMOS (Tateuchi et al. 2012b). Although there is no Paα line profile measured in local LIRGs, velocity dispersion of $\sigma = 150$ km s^{-1} is reasonable because the value is consistent with those derived for Hα lines of local LIRGs (Alonso-Herrero et al. 2009). Dispersion of differences in the fluxes between those obtained from HST/NICMOS and from our method is 12.2% (Tateuchi et al. 2012b).

Figure 2 shows the assumed intrinsic emission-line profile (dashed line), atmospheric transmittance (solid line), and estimated emission-line profile affected by the atmospheric absorption (dark-shaded area). The factor $T_{\rm line}$ within the bandpass $[\lambda_1,\ \lambda_2]$ of the $N191$ filter is then calculated as follows;

$$T_{\rm line} = \frac{\int_{\lambda_1}^{\lambda_2} \exp\left[-\left(\frac{\lambda-(1+z)\lambda_{\rm Pa\alpha}}{\sqrt{2}\sigma}\right)^2\right] T_{\rm atm}(\lambda)d\lambda}{\int_{\lambda_1}^{\lambda_2} \exp\left[-\left(\frac{\lambda-(1+z)\lambda_{\rm Pa\alpha}}{\sqrt{2}\sigma}\right)^2\right] d\lambda}, \qquad (2)$$

where z is the redshift obtained from $IRAS$ RBGS catalog (Sanders et al. 2003), $T_{\rm atm}(\lambda)$ represents the model atmospheric transmittance curve, and $\lambda_{\rm Pa\alpha}$ is the intrinsic wavelength of Paα (1.8751 μm).

In Table 2, calculated Paα fluxes as well as $(T^{\rm PWV,N191}_{\rm atm})^X$ and $T_{\rm line}$ estimated by our method are listed. The median value of the PWV is 0.5 mm during our observation.

4. RESULTS

4.1. *Final Images*

In Figure 3, all of our 44 individual galaxies in 38 systems are shown. The continuum images made by interpolating the H and $K_{\rm s}$ images are shown on the left side and the Paα line images, which is derived by subtracting continuum image from the $N191$ image, on the right.

4.2. *Paα Flux*

To estimate a total Paα flux of a galaxy, we first estimate how extended emission-line distributions are. Because there are large diversity in Paα morphology, we use isophotal photometry technique for our image, where 5σ isophotal area above the sky background level for Paα image is used. The 1σ noise level is measured in each Paα image convolved with a Gaussian function with a FWHM of 8 pixels to reduce the noise level, and the 5σ area is defined in this convolved line image.

The results are shown in Table 2 and Figure 3. Photometric uncertainties, $\sigma({\rm Pa}\alpha)_{\rm phot}$, are defined as 1σ noise level measured by applying many apertures having the same area size as that used for the measurement of the total Paα flux at blank sky positions. These values are not so large ($\sim 0.5\%$ on average). The $\sigma({\rm Pa}\alpha)_{\rm atm}$ is an error due to our Paα correction method mentioned in Section 3 and set to be 12.2% (Tateuchi et al. 2012b). We use the combination of them,

$$\sigma_{\rm total} = \sqrt{\sigma({\rm Pa}\alpha)^2_{\rm phot} + \sigma({\rm Pa}\alpha)^2_{\rm atm}}, \qquad (3)$$

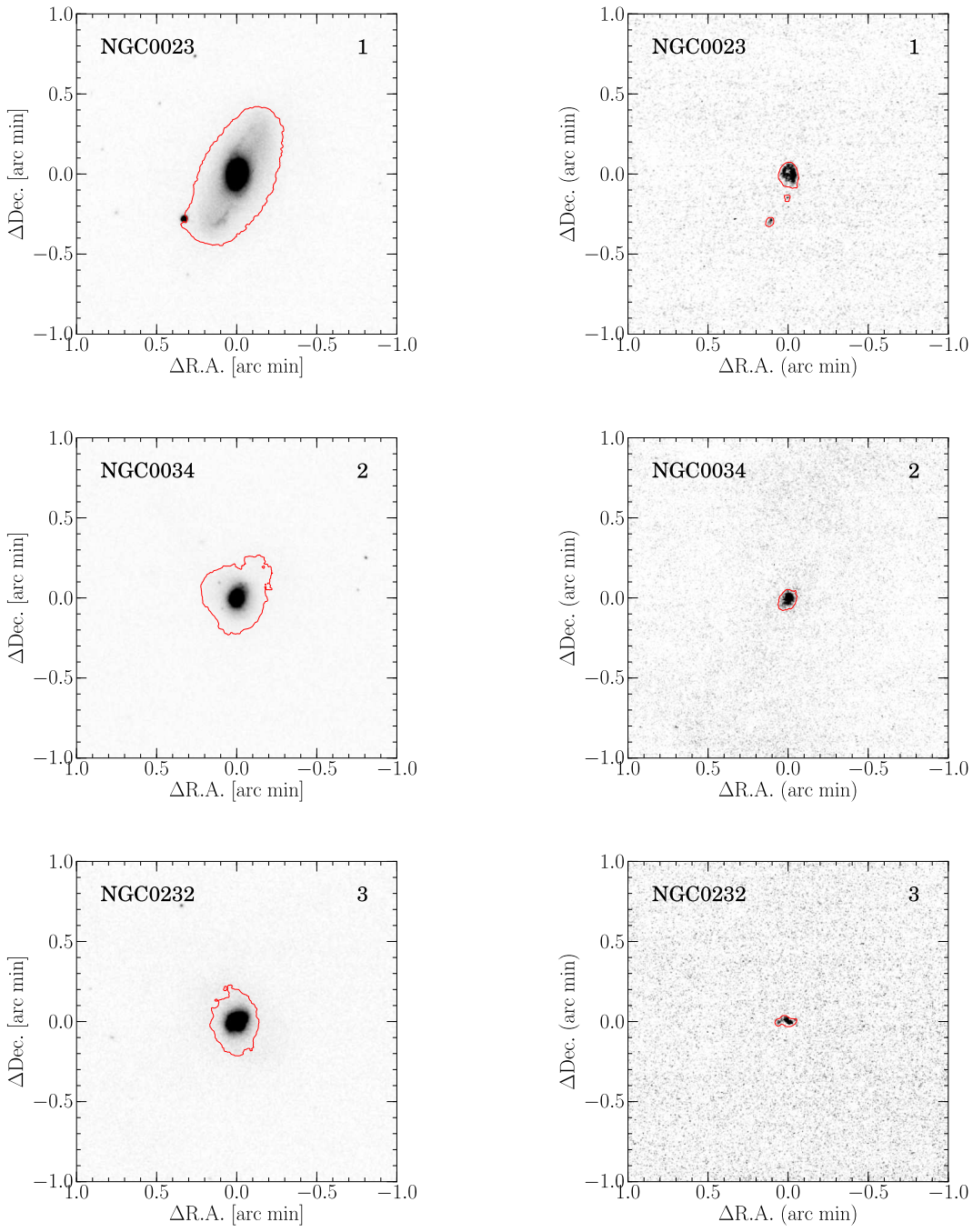

FIG. 3.— Continuum and Paα line images of our sample of 44 individual LIRGs in 38 systems observed with miniTAO/ANIR. The continuum images are listed on the left side and Paα line images on the right. The name of a galaxy is shown at the top-left corner and ID number at the top-right corner in each figure. The solid red lines represent 10σ surface brightness level for the continuum image and 5σ for the Paα line image measured on convolved images. The 1σ levels are calculated on the convolved images (see text).

as the total uncertainties on the measurement of the Paα flux.

Our results may miss any diffuse Paα emission whose surface brightness is lower than the 5σ threshold. In the *HST*/NICMOS images, missing the diffuse Paα flux is also pointed out by Alonso-Herrero et al. (2006). In order to evaluate the maximum missing flux of Paα line emission ($f(\mathrm{Pa}\alpha)_{\mathrm{miss}}$), we assume the diffuse emission is spread over an aperture, whose area is defined by 10σ isophote for each continuum image. Then, the amount of the missing diffuse component is estimated to be 1.8% on average at a maximum.

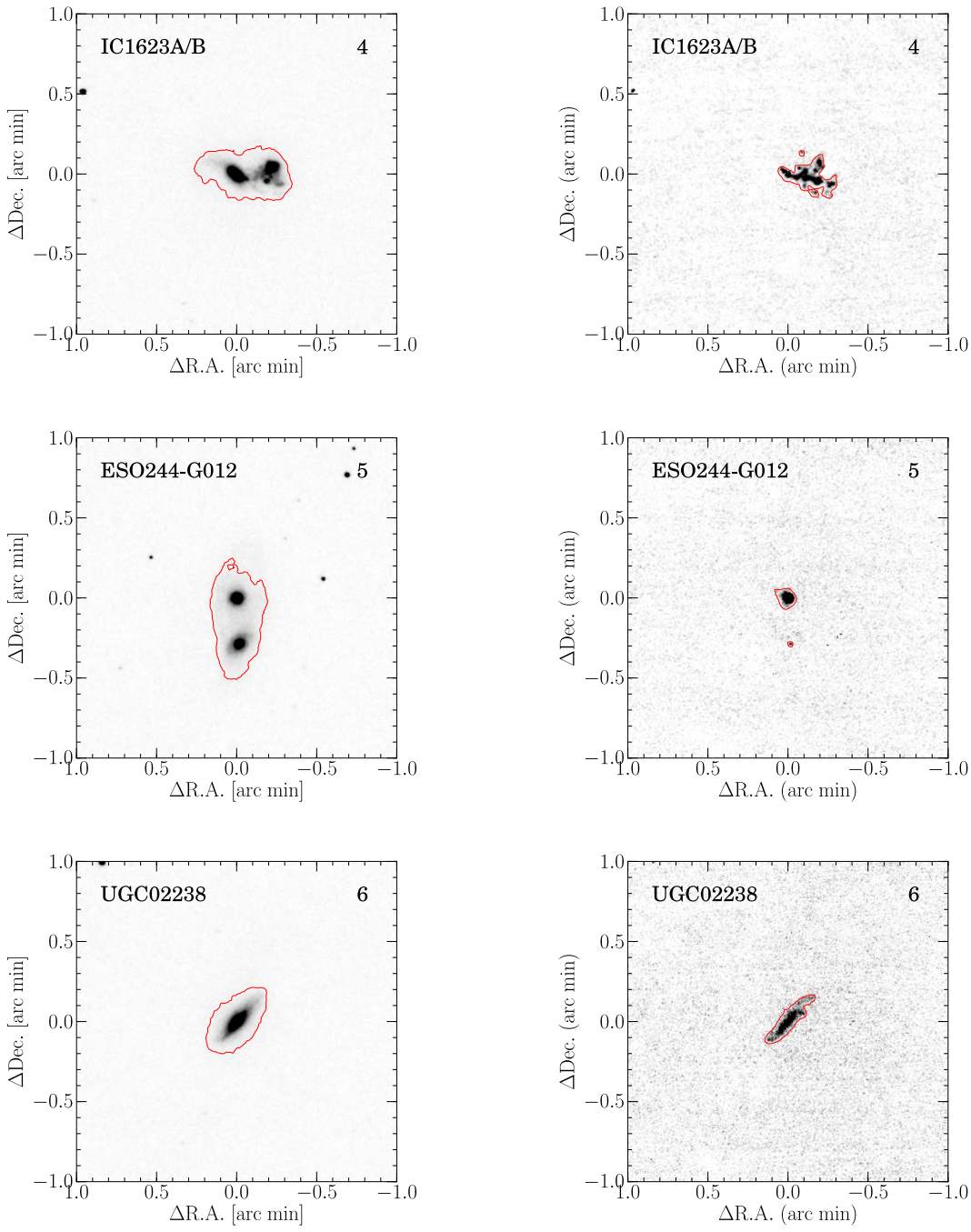

FIG. 3.— Continued

4.3. *Notes on Individual Objects*

Following are notes on the individual galaxies, where the number at the top represents our sample ID. Continuum and $N191$ images are shown in Figure 3.

1. NGC 23 (IRAS F00073+253; Mrk 545): This is a paired galaxy with NGC 26 (Alonso-Herrero et al. 2006) at a distance of 9′.1. It is a barred spiral (Sa; HyperLeda[1]) classified as an HII galaxy by a long-slit spectroscopic study (Veilleux et al. 1995). X-ray emission is not detected by Swift/BAT (Koss et al. 2013). A ring starburst region are detected at the center of the galaxy. In addition to this structure, we find an extended Paα emission-line region along the southern spiral arm which is located outside the field of view of the *HST*/NICMOS observation.

[1] database for physics of galaxies; http://leda.univ-lyon1.fr (Paturel et al. 2003)

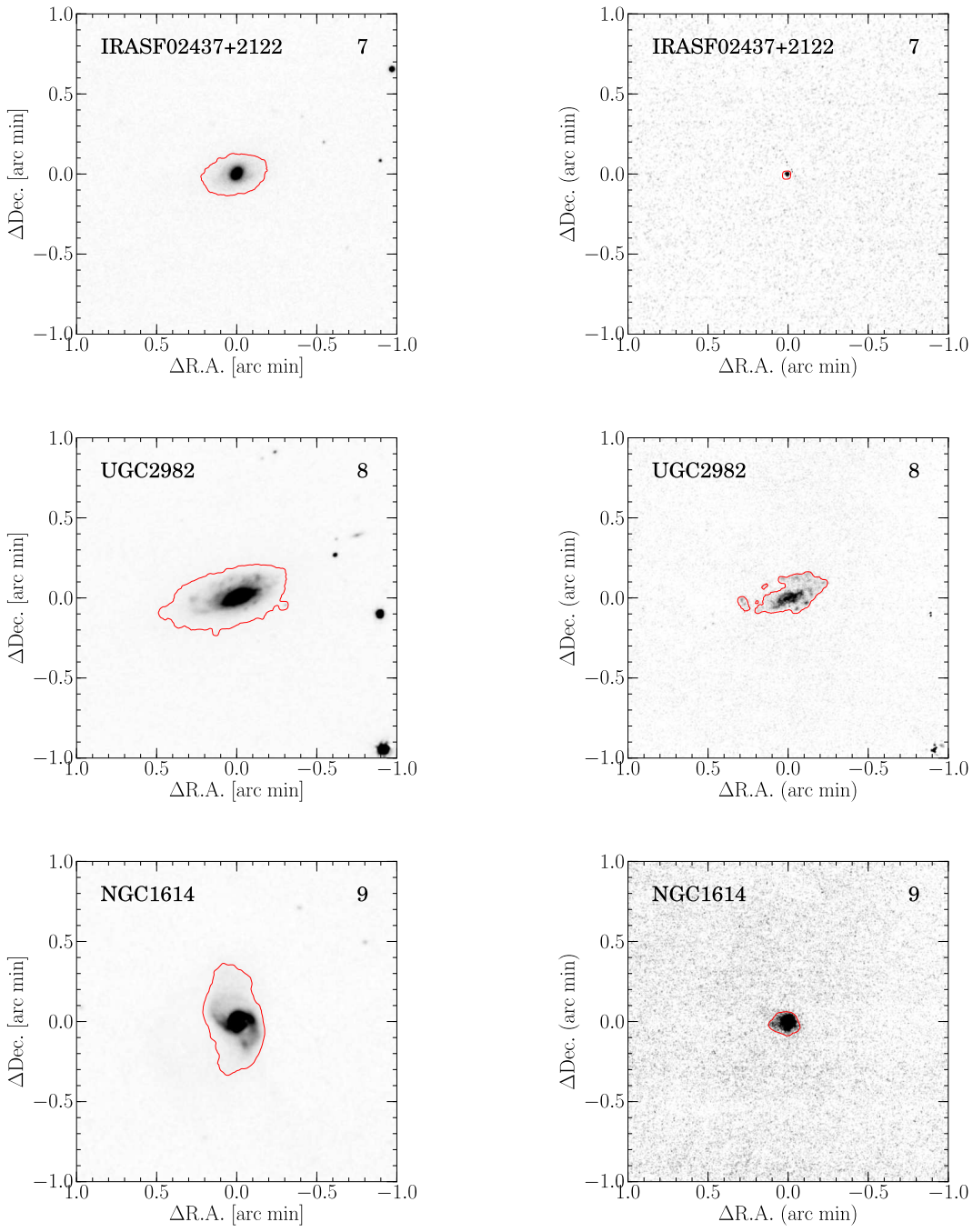

FIG. 3.— Continued

2. NGC 34 (IRAS F00085−1223; Mrk 938; VV 850): This galaxy, hosting a strong starburst and a weak AGN, as evidenced by its optical, infrared, radio, and X-ray properties, is known as a remnant of unequal gas-rich merger (e.g., Fernández et al. 2010; Schweizer & Seitzer 2007). It is an S0/a (HyperLeda) and classified as a Seyfert 2 by a long-slit spectroscopic study (Veilleux et al. 1995). Paα emission-line region is concentrated at the center of the galaxy.

3. NGC 232 (IRAS F00402−2349; VV 830; AM 0040-234): This has a companion galaxy (NGC 235) at a distance of 2′. It is a barred spiral (SBa; HyperLeda) classified as an HII galaxy (Corbett et al. 2003; Veilleux et al. 1995). HII blobs, suggested as optical debris, between these two galaxies are detected in Hα (e.g., Dopita et al. 2002; Richter et al. 1994), but the Paα data is not enough deep to detect the blobs. While NGC 232 has bright FIR emission, NGC 235 has no FIR flux though it has bright HII blobs (Richter et al. 1994).

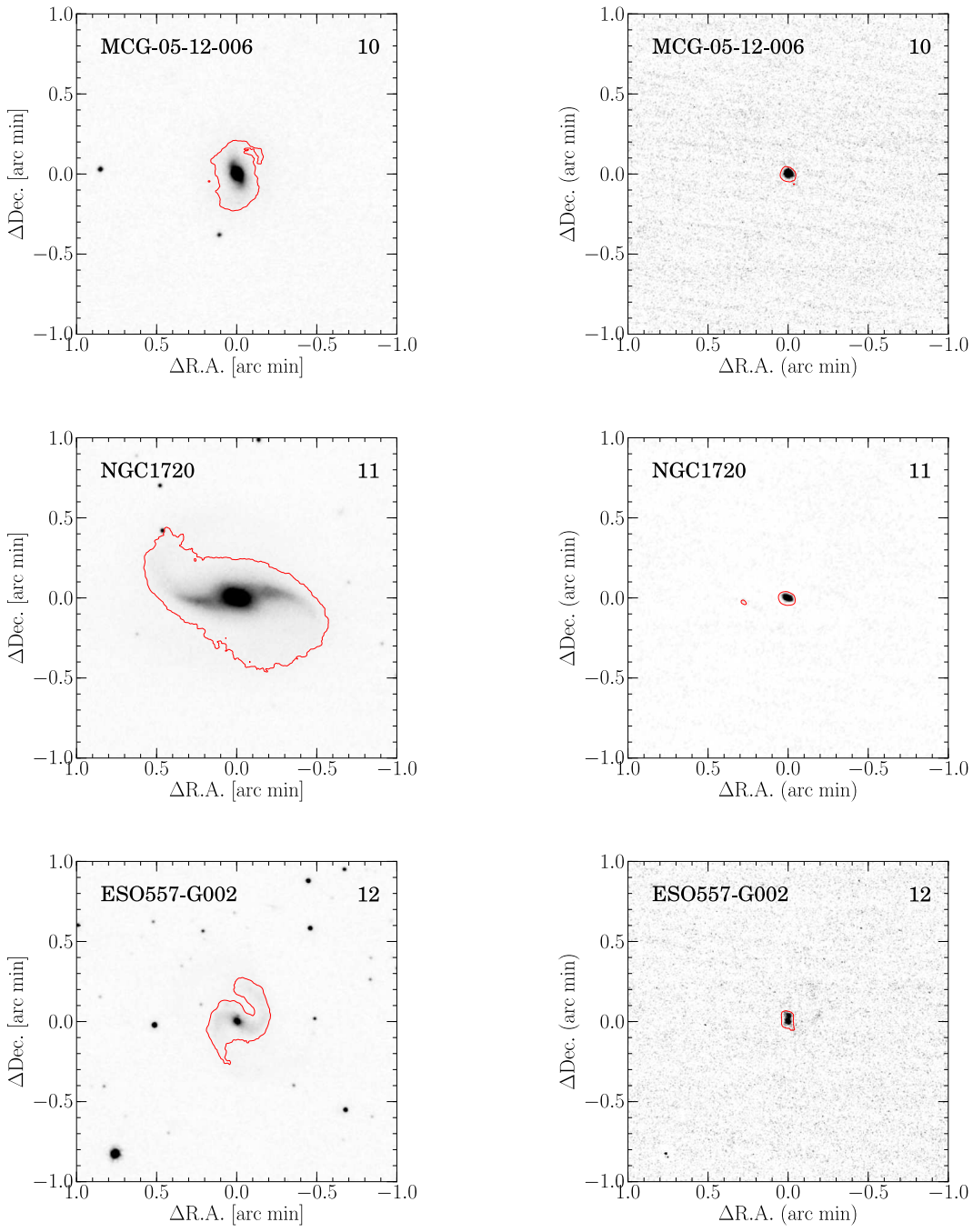

FIG. 3.— Continued

4. IC 1623A/B (IRAS F00402−2349; VV 114; Arp 236): This system is known as a merger at its middle or late stage, and consists of two galaxies, IC 1623B and IC 1623A. An obscured AGN in IC 1623B is revealed by MIR spectroscopy and X-ray observations (e.g., Alonso-Herrero et al. 2002; Grimes et al. 2006) suggesting that both starburst and AGN activities might be triggered by the ongoing merger. These galaxies are classified as an HII galaxy (Corbett et al. 2003; Veilleux et al. 1995). The diffuse component of Paα emission is distributed between the two galaxies over 10 kpc (Iono et al. 2013; Saito et al. 2013).

5. ESO 244-G012 (IRAS F01159−4443; VV 827; AM 0115-444): This system is on-going interacting paired galaxies (Agüero et al. 2000), separated by 17″. Both are spirals (Sc; HyperLeda), and the northern galaxy is classified as an HII galaxy (Corbett et al. 2003), while the class of the southern galaxy is ambiguous (Corbett et al. 2003). The northern galaxy has bright con-

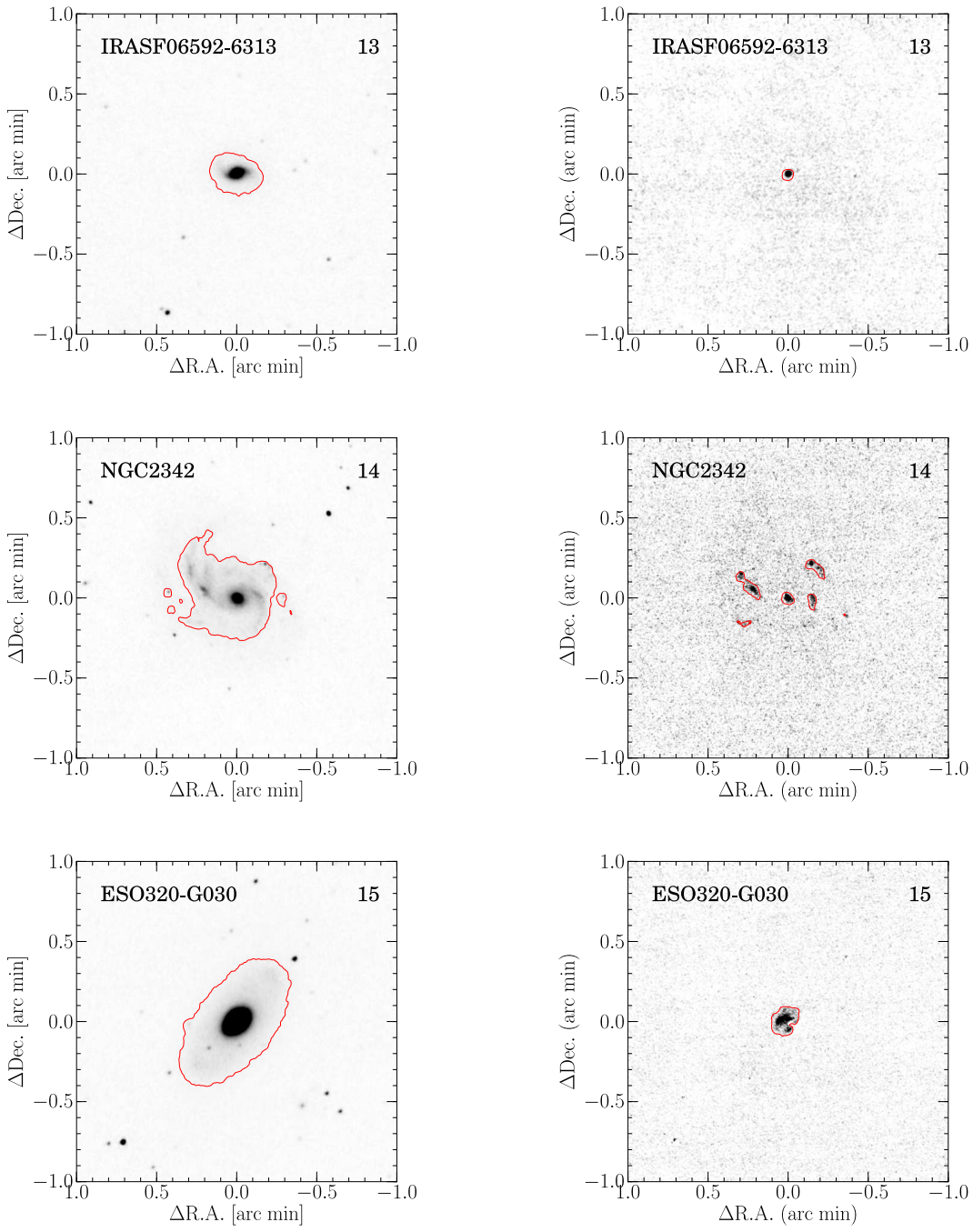

FIG. 3.— Continued

centrated Paα emission at its center, while the southern source is faint.

6. UGC 2238 (IRAS F02435+1253): This object is known as a merger remnant, and it is questionable whether it is undergoing or has undergone any amount of violent relaxation (Rothberg & Joseph 2004). It is an edge-on disk galaxy (Sm; HyperLeda) classified as a LINER (Veilleux et al. 1995). Strong Paα emission are detected not only from the central region, but also from the disk component.

7. IRAS F02437+2122: This is an elliptical galaxy (E; HyperLeda) classified as a LINER (Veilleux et al. 1995). X-ray emission is detected (S/N=2.7, $L_{14-195\mathrm{keV}} < 10^{42.9}$ (erg s^{-1})) by Swift/BAT (Koss et al. 2013), but no high-quality X-ray data is obtained. The Paα morphology is compact and concentrated at the central region.

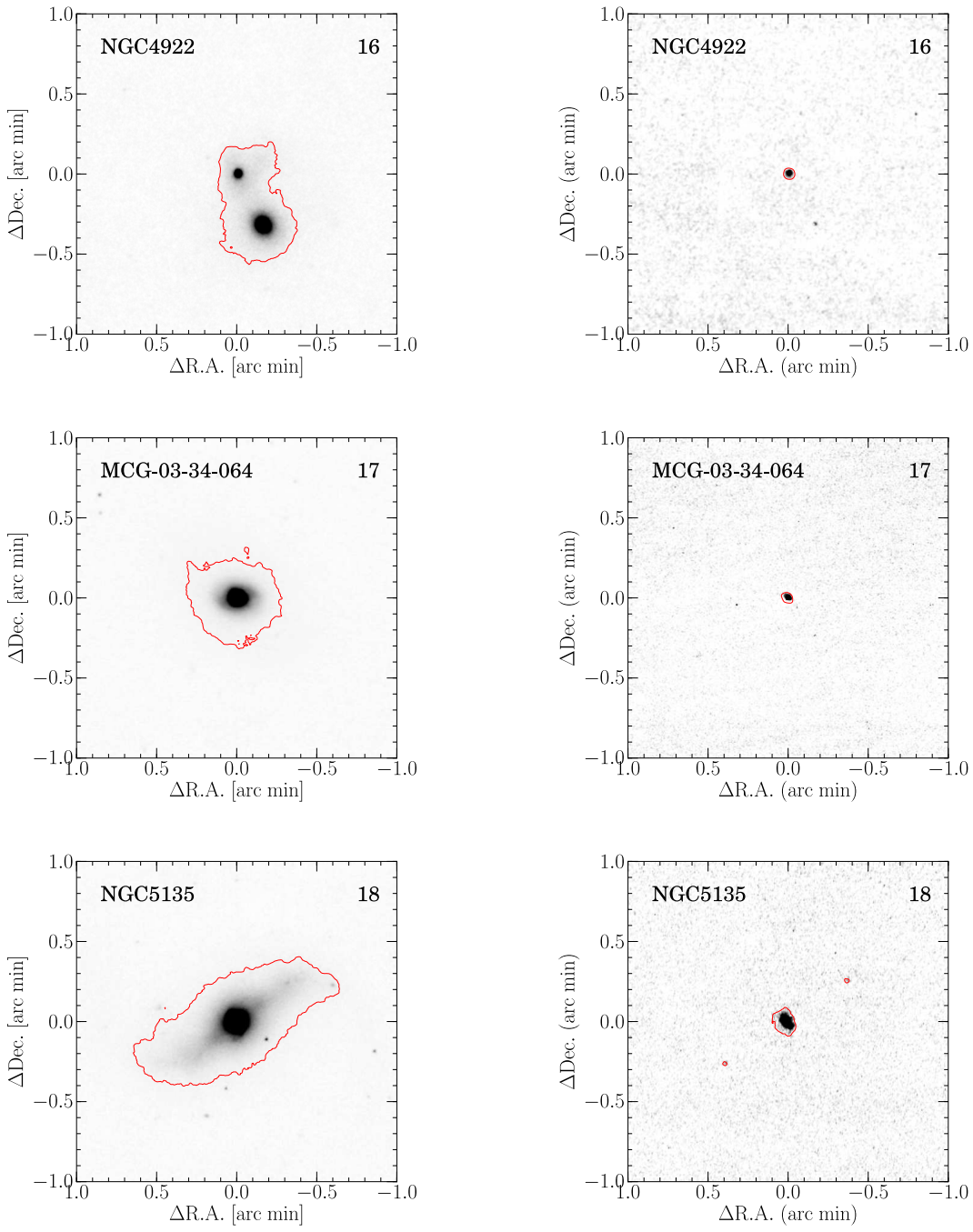

FIG. 3.— Continued

8. UGC 2982 (IRAS F04097+0525): This is a barred spiral (SABa; HyperLeda) classified as an HII galaxy by a long-slit spectroscopic study (Veilleux et al. 1995). It is a diffuse isolated system having extended HII gas (Chaboyer & Vader 1991) and 850 μm emission extends to the periphery of a optical disk (Thomas et al. 2004). Paα emission-line region is also extended out to the disk with clumpy blobs.

9. NGC 1614 (IRAS F04315−0840; ARP 186; Mrk 617; IIZW 015): This is a well known merger at its late stage, and found to be a minor merger system with a mass ratio of 5:1∼3:1 (Väisänen et al. 2012). It is a barred spiral (SBc; HyperLeda) classified as an HII galaxy (Veilleux et al. 1995; Alonso-Herrero et al. 2001; Corbett et al. 2003). A tidal tail can be seen in our continuum image, which is consistent with other broad-band images (Dopita et al. 2002; Rodríguez-Zaurín et al. 2011). A ring-like structure surrounding a nuclear region is discovered in a Paα image with *HST*/NICMOS

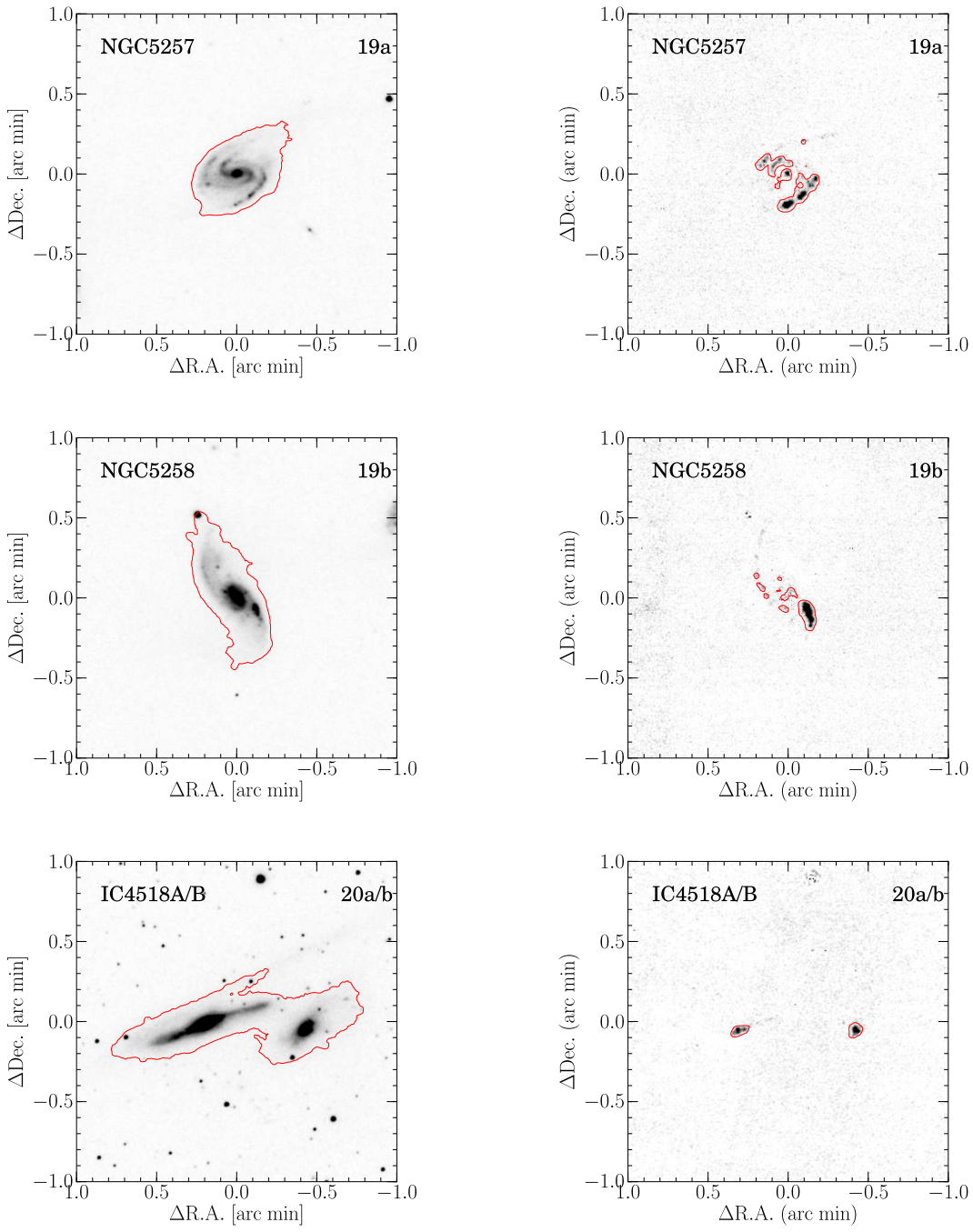

FIG. 3.— Continued

(Alonso-Herrero et al. 2001). An extended star-forming region is detected in the Paα image, but the ring-like structure can not be detected in the 0.″8 spatial resolution of ANIR. Alonso-Herrero et al. (2001) describes that the growth of the ring structure is "inside-out", but Olsson et al. (2010) suggests that the ring is the result of a resonance.

10. MCG −05-12-006 (IRAS F04502−3304): This is an isolated barred spiral (SBb; HyperLeda) with a tidal tail (Yuan et al. 2010) and classified as an HII galaxy (Yuan et al. 2010). Paα emission is compact and concentrated at the center of the galaxy.

11. NGC 1720 (IRAS F04569−0756): This is a paired galaxy with NGC 1726 at a distance of 8.″2. It is a barred spiral (SBab; HyperLeda), but its energy source is not identified. The Paα emission is concentrated at the center of the galaxy, and little emission can be seen at the spiral arm.

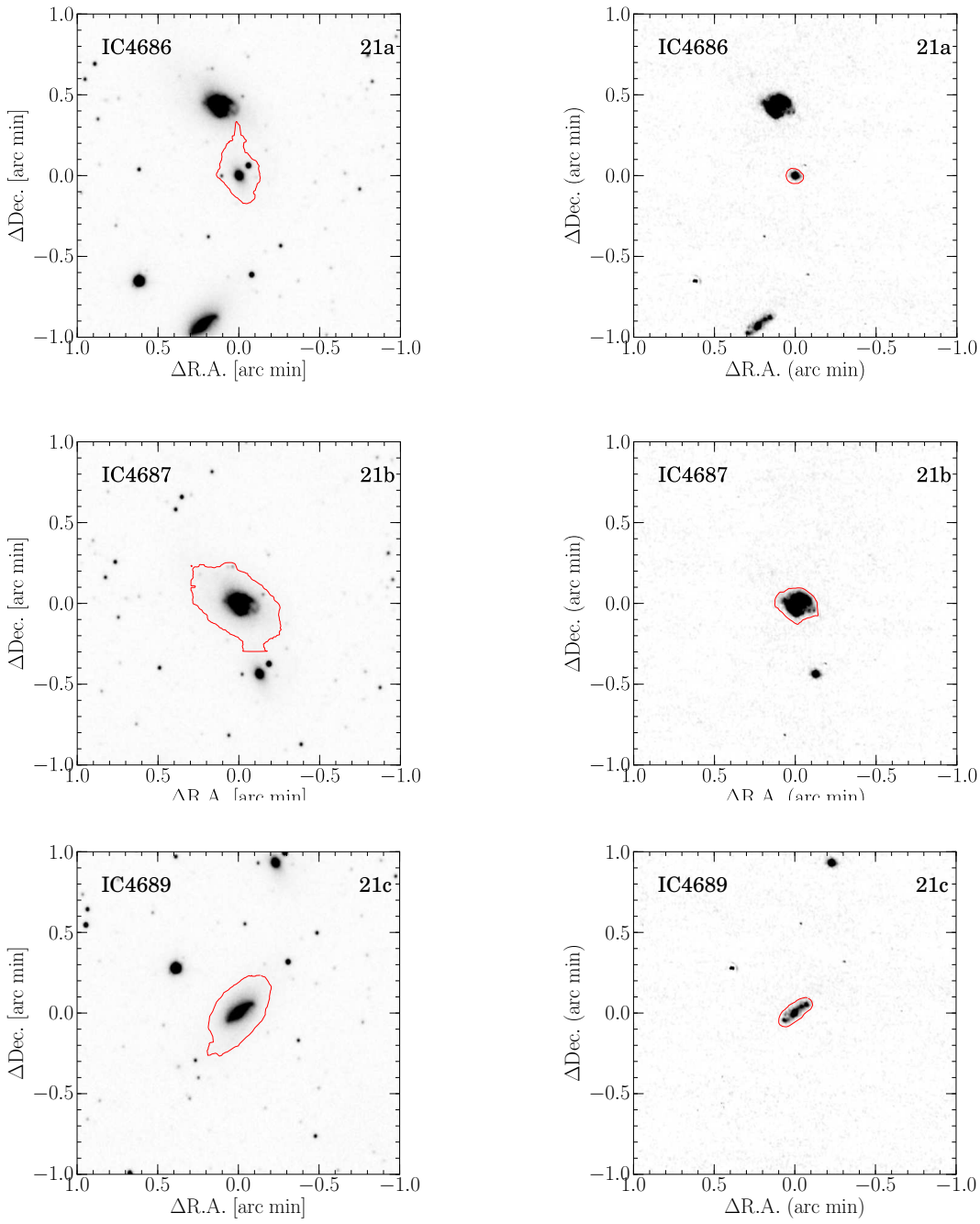

FIG. 3.— Continued

12. ESO 557-G002 (IRAS F06295−1735): This galaxy has a companion galaxy (ESO 557-G001) at a distance of 1.′6 towards the south. It is a barred spiral (SBbc; HyperLeda) classified as an HII galaxy by a long-slit spectroscopic study (Corbett et al. 2003). Ultra-hard X-ray (14-195 keV) emission cannot be detected by Swift/BAT (Koss et al. 2013). The companion shows tidal distortion in the R-band and an Hα image (Dopita et al. 2002) but does not show clearly in the K_s-band and the Paα image. Two strong concentrated peaks at the center of the galaxy is detected on the Paα image.

13. IRAS F06592−6313: This is an isolated barred spiral (SABb; HyperLeda) with a tidal tail (Yuan et al. 2010) classified as an HII galaxy (Yuan et al. 2010). It has Hα condensation outside its main body at 7.″0 towards the north (Rodríguez-Zaurín et al. 2011), of which the Paα image is not enough deep to detect. Distribution of Paα emission is concentrated at the center of the galaxy.

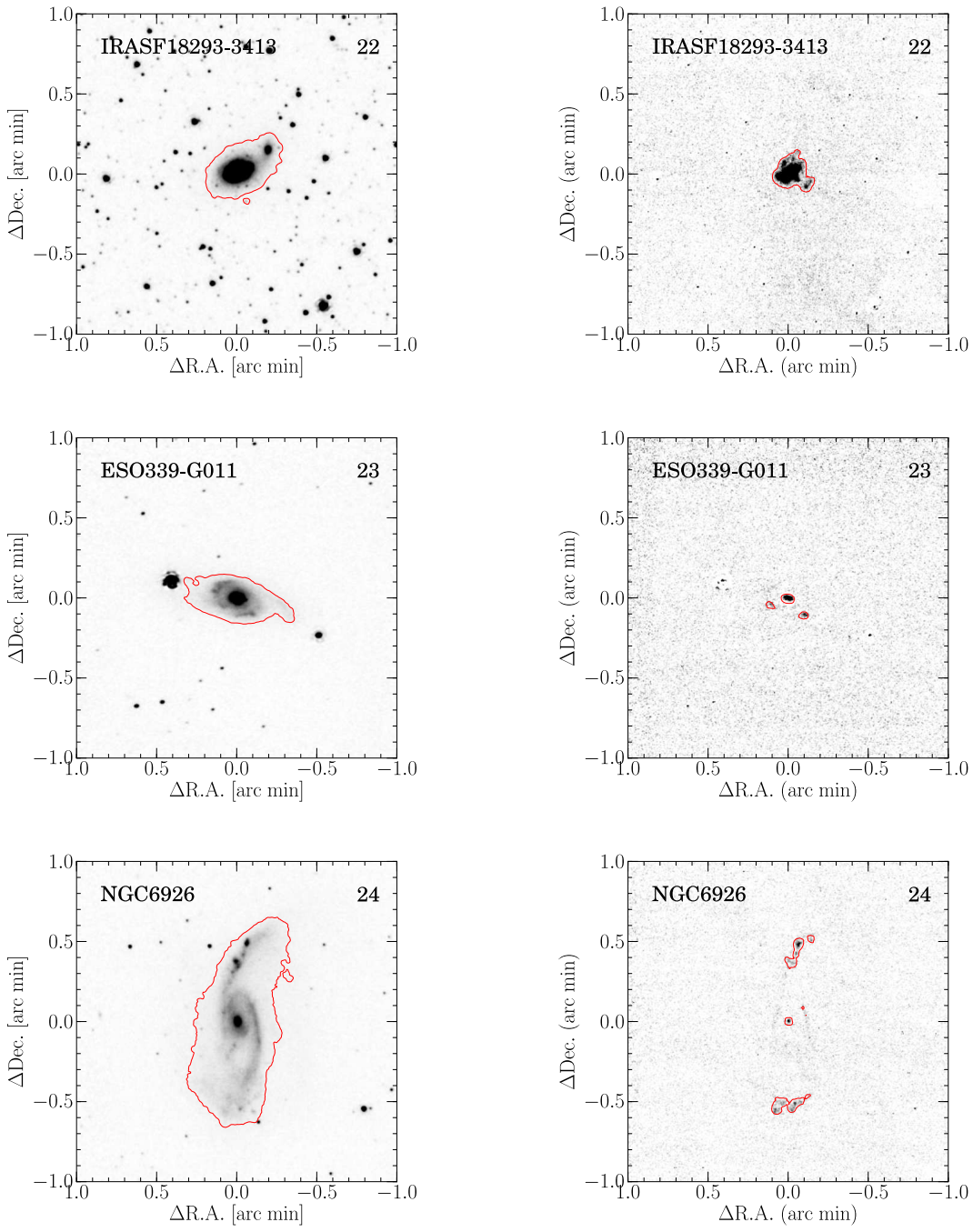

FIG. 3.— Continued

14. NGC 2342 (IRAS 07063+2043): This is a spiral (Sc; HyperLeda) classified as an HII galaxy (Ho et al. 1997) without an AGN activity at any wavelength, having a paired galaxy (NGC 2341; Alonso-Herrero et al. 2006) at a distance of 2.′5. This is not a well studied pair (Jenkins et al. 2005). The both galaxies have high IR luminosities of $\log(L_{\rm FIR}/L_{\odot}) = 10.8$ (Sanders et al. 2003). Paα emission is extended along the spiral arms over 10 kpc.

15. ESO 320-G030 (IRAS F11506−3851): This is a barred spiral (SBb; HyperLeda) classified as an HII galaxy (van den Broek et al. 1991). VLT-VIMOS/Hα (Rodríguez-Zaurín et al. 2011) and *HST*/NICMOS Paα (Alonso-Herrero et al. 2006) observations report starburst regions distributed in a ring-like shape, while they can not be seen in continuum images. In the Paα image, the same ring structure can be seen, and the emission line region is extended beyond the ring.

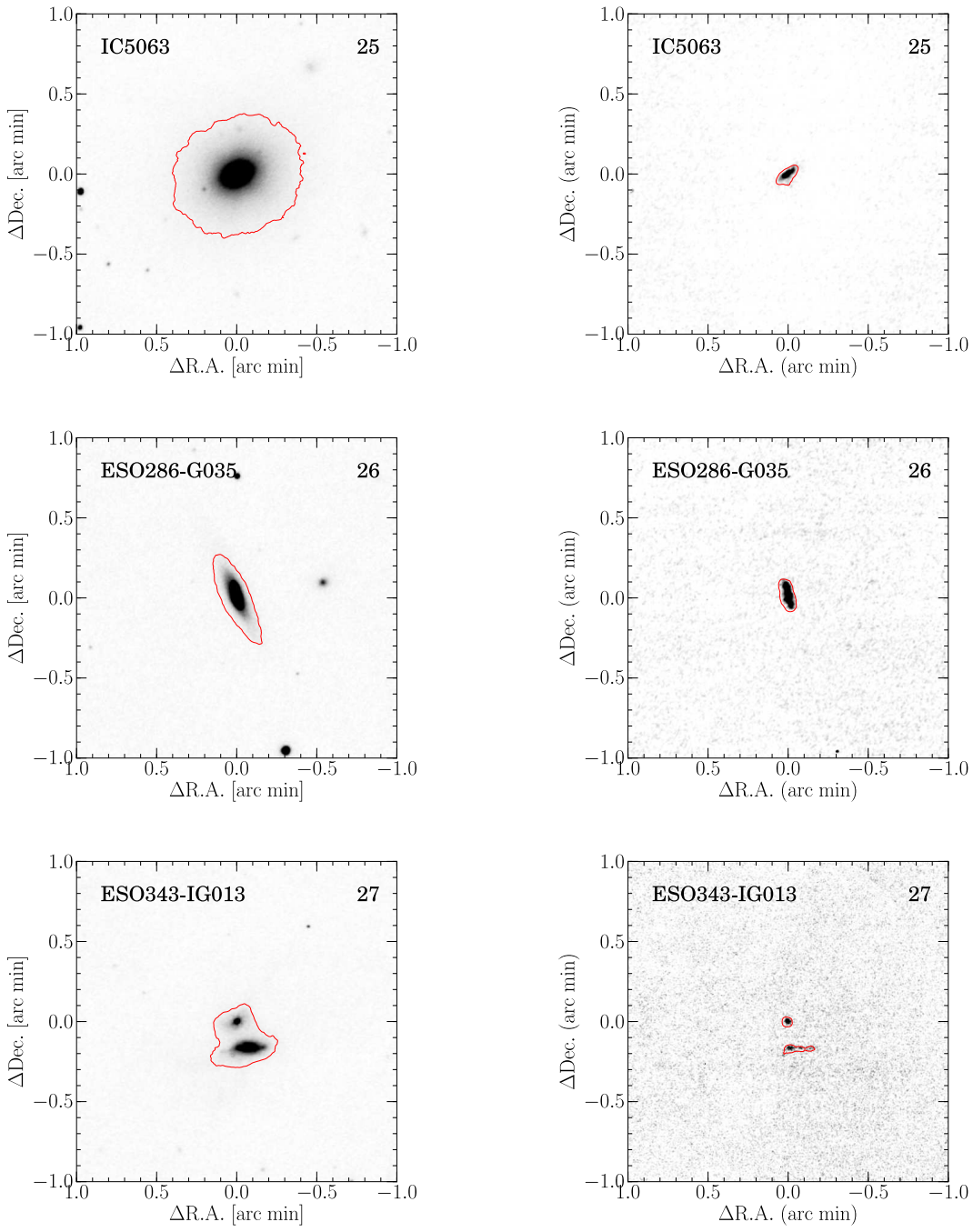

FIG. 3.— Continued

16. NGC 4922 (IRAS F12590+2934; VV 609; KPG 363A/B): This is known as a post-merger between an early-type and a spiral, located at the outskirts of the Coma cluster (Sheen et al. 2009). It is an elliptical (E; HyperLeda) classified as a LINER (van den Broek et al. 1991), and shows extended soft X-ray emission not originated from an AGN but possibly related to the on-going star formation (Alonso-Herrero et al. 1999) in the northern galaxy, especially. In the Paα image, the concentrated northern nucleus has strong and extended emission, but the southern one is faint.

17. MCG −03-34-064 (IRAS F13197−1627): This galaxy forms a wide binary system with MCG −03-34-063 (Yuan et al. 2010), and is an S0/a (Naim et al. 1995) classified as a Seyfert 1 spectroscopically (Véron-Cetty & Véron 2006). Paα emission is compact and concentrated at the center of the galaxy. In addition, a paired galaxy located 1.′8 away are found have a compact Paα source.

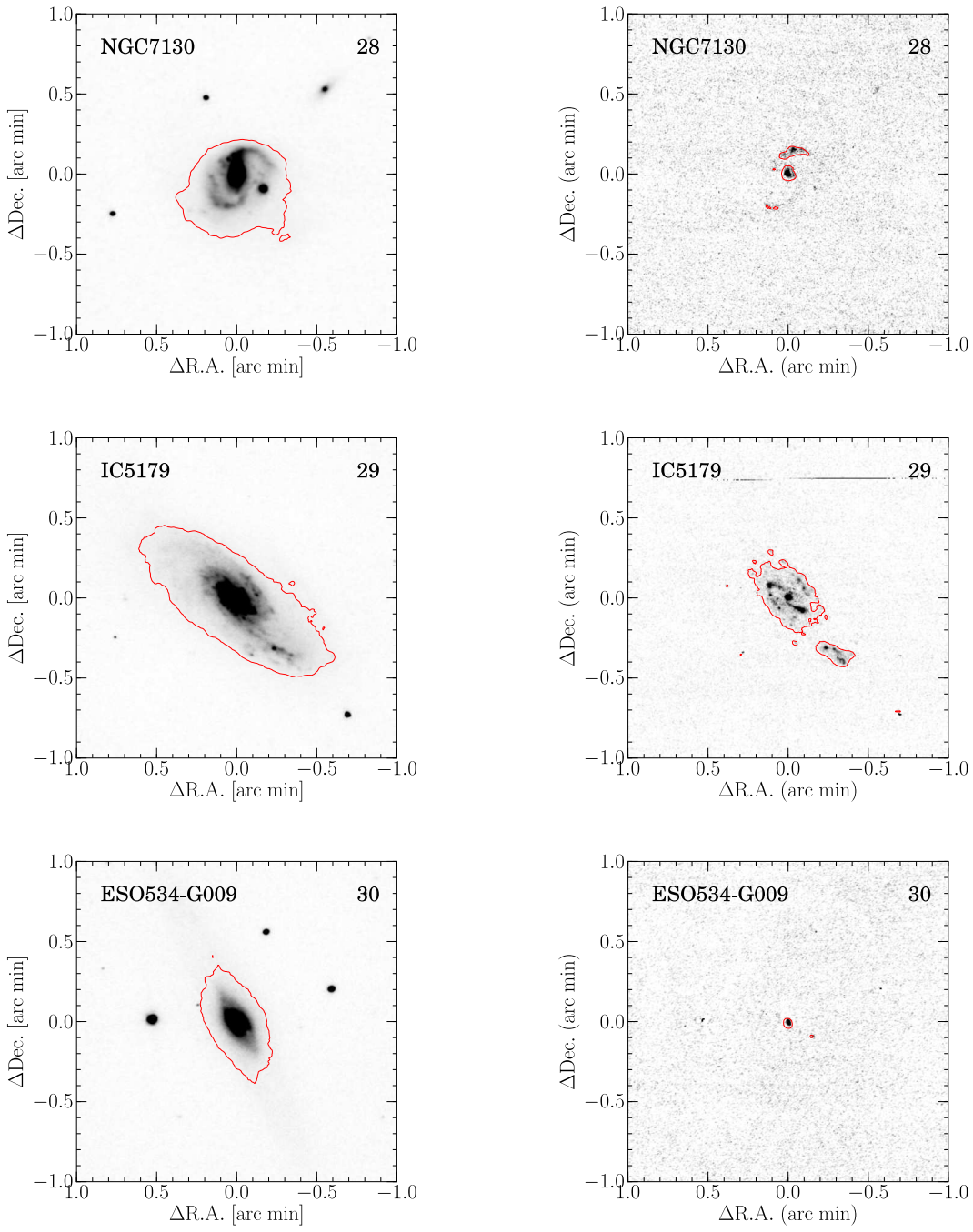

FIG. 3.— Continued

18. NGC 5135 (IRAS F13229−2934): This galaxy is an isolated system (Yuan et al. 2010), and is an SB(s)ab (de Vaucouleurs et al. 1991) classified as a Seyfert 2 (Corbett et al. 2003). In the Paα image, clumpy blobs are detected at the central region which have been already reported in previous Hα and Paα imaging observations (e.g., Rodríguez-Zaurín et al. 2011; Alonso-Herrero et al. 2006). Also, a mini-spiral structure can be seen in our Paα image.

19. NGC 5257/8 (IRAS F13373+0105 NW/SE; Arp 240; VV 055; KPG 389): These galaxies form an interacting pair with a separation of 1.′3. NGC 5258 is an SA(s)b; peculiar, and NGC 5257 is an SAB(s)b; peculiar (de Vaucouleurs et al. 1991) both are classified as HII galaxies (Corbett et al. 2003; Veilleux et al. 1995). While a tidal tail between these galaxies can be seen in the continuum image, Paα emission is not detected there, which is consistent with Hα imaging observations (Dopita et al. 2002). NGC 5257 has Paα blobs along the

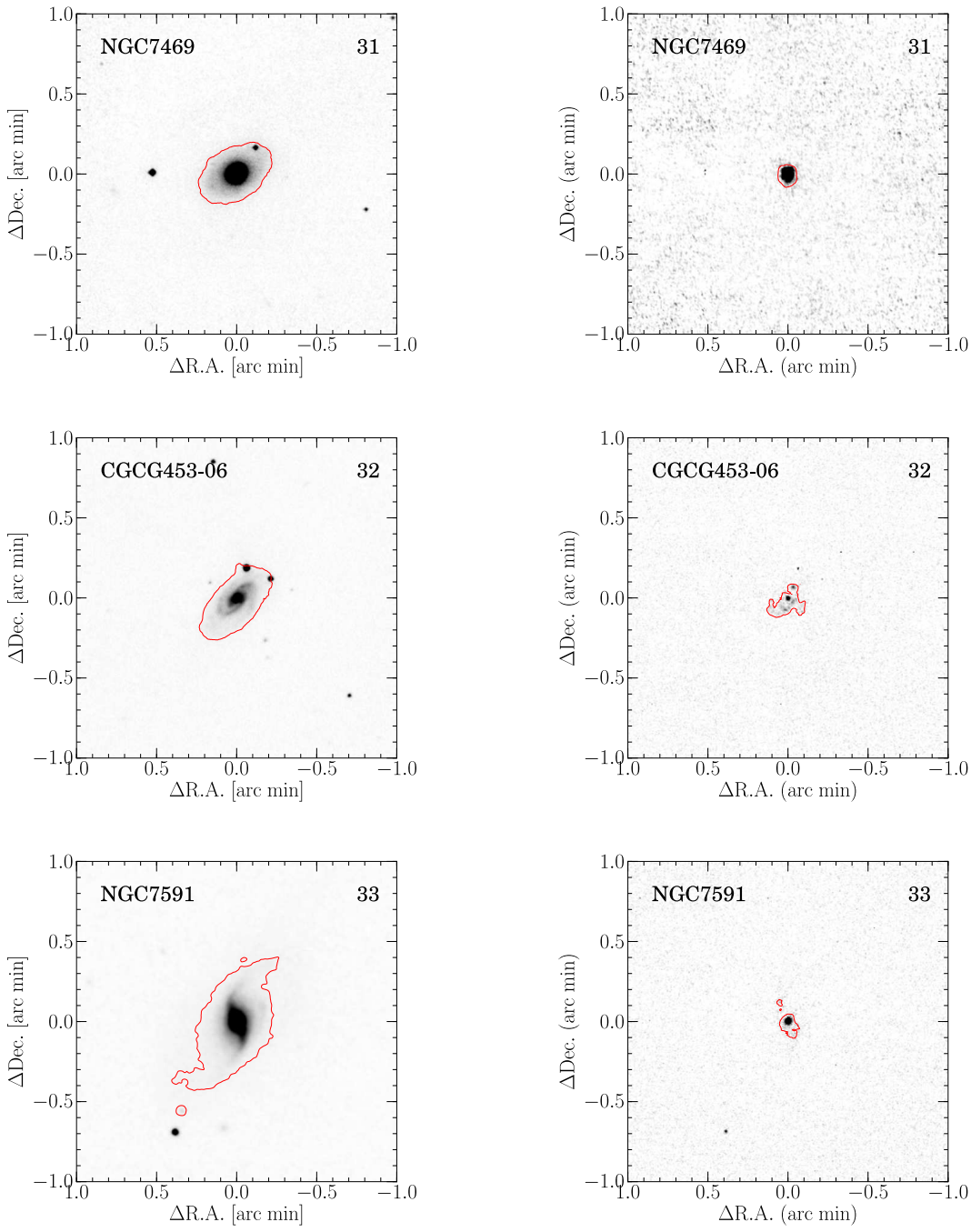

FIG. 3.— Continued

spiral arms and the southern arm has stronger and bigger clumps of emission. NGC 5258 also has Paα blobs along spiral arms, with the southern arm having stronger Paα emission where larger amount of CO(1 − 0) emission is detected (Iono et al. 2005).

20. IC 4518A/B (IRAS F14544−4255; VV 780; AM 1454−425): This is a strongly interacting pair of galaxies with a separation of 37.″6. Both are spirals (Sc; HyperLeda) classified as Seyfert 2 (Corbett et al. 2003). Although tidal tails exist not only between these galaxies but also at spiral arms of each galaxy as can be seen in the continuum image, the Paα emission is not detected there, being consistent with Hα imaging observations (Dopita et al. 2002). While the western galaxy has a strong and concentrated Paα emission at the central region, the eastern galaxy has extended Paα emission not only at its center but also along its spiral arms.

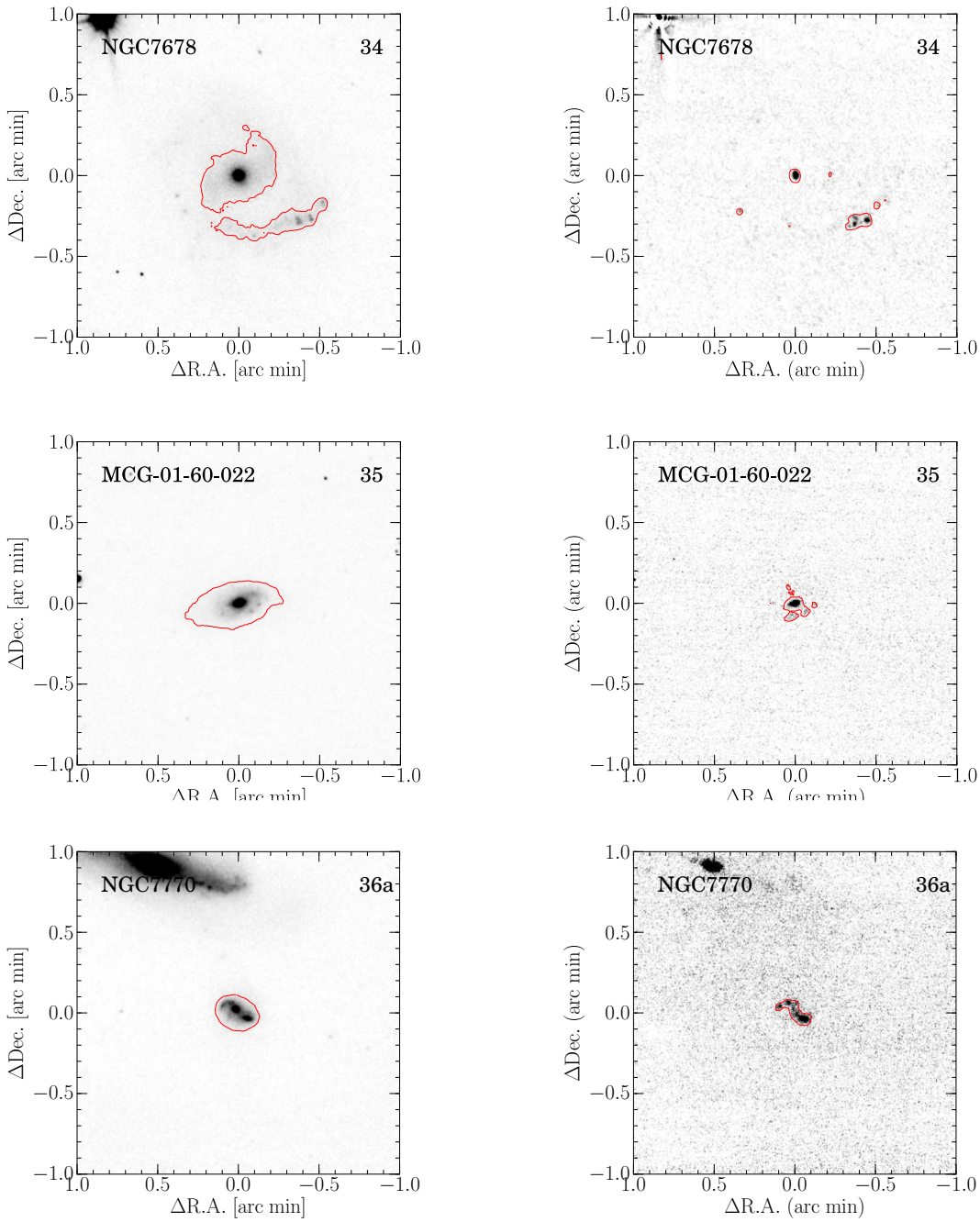

FIG. 3.— Continued

21. IC 4687/6 (IRAS F18093−5744; AM 1809−574): This is a system of three interacting galaxies (IC 4687; IC 4686; IC 4689) (West 1976). The separation between the northern (IC 4687) and center (IC 4686) galaxy is 27.″8, and between the center and the southern (IC 4689) galaxy is 56.″8. The northern galaxy is a barred spiral (SABb; HyperLeda), the center is an elliptical (E; HyperLeda), and the southern is a barred spiral (SABa; HyperLeda), all classified as an HII galaxies (Yuan et al. 2010; Veilleux et al. 1995). These galaxies show strong Paα emission; the northern galaxy has disturbed blobs like a ring starburst, which is consistent with a Paα image of *HST*/NICMOS (Alonso-Herrero et al. 2006), the central galaxy has concentrated Paα emission at the center, and the southern galaxy has extended emission regions along the spiral arms. We can not see the Paα emission between these galaxies, which is consistent with Hα imaging observations (Rodríguez-Zaurín et al. 2011; Dopita et al. 2002).

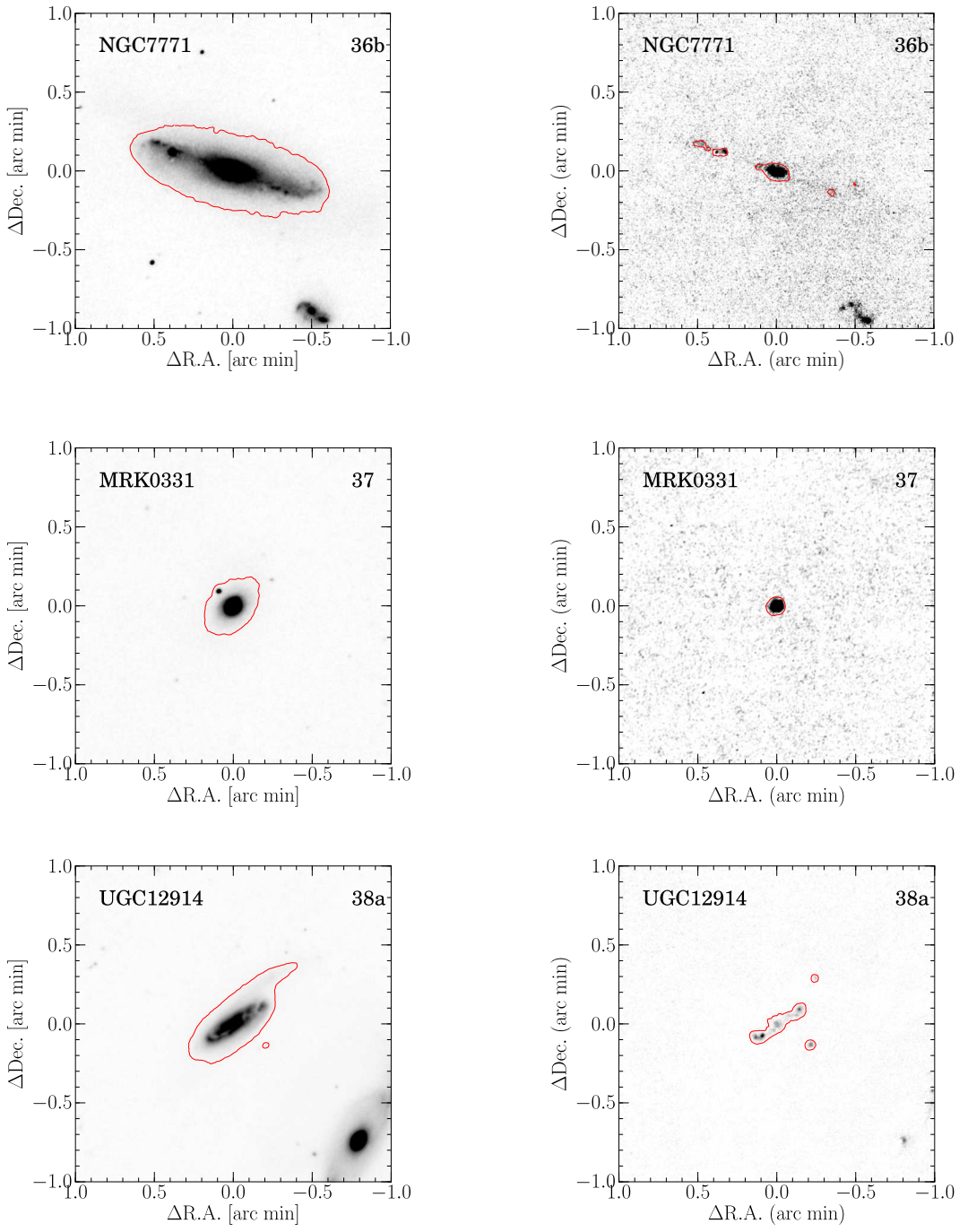

FIG. 3.— Continued

22. IRAS F18293−3413: This galaxy is an S0/a (HyperLeda) classified as an HII galaxy (Veilleux et al. 1995). It shows a concentrated Paα emission region at the center and diffuse region along the disk.

23. ESO 339-G011 (IRAS F19542−3804): This is an isolated barred galaxy (SBb, HyperLeda) with a tidal tail (Yuan et al. 2010) classified as a Seyfert 2 (Yuan et al. 2010). It has disturbed Paα emission at the center and some blobs can be detected along the disk. It seems to have a companion with a separation of 14.″3 with a tidal tail. The Paα emission region possibly were induced by merger, but the emission can not be detected in the companion.

24. NGC 6926 (IRAS F20305−0211; VV 621): This is a barred galaxy (Sc; HyperLeda) and has a companion of dwarf elliptical (NGC 6929) at a distance of ∼ 4′ towards east. The starburst activity of this galaxy has presumably been triggered by a M51-type density wave

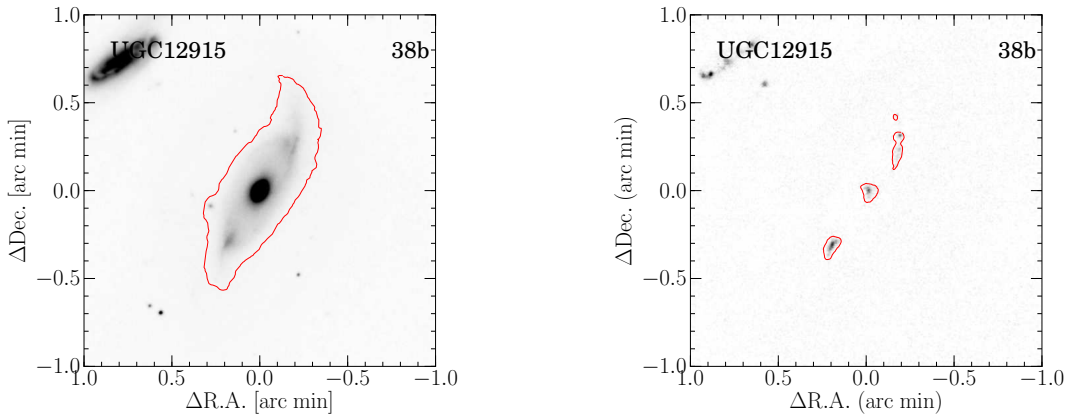

FIG. 3.— Continued

induced by the companion (Lutz 1991). This is classified as a Seyfert 2 (Veilleux et al. 1995) or an HII galaxy (Corbett et al. 2003). While strong Hα emissions are seen along the spiral arms especially in the northern part, no emission is detected in the nucleus (Dopita et al. 2002). However, bright Paα emission is detected not only at the spiral arms but also in the nucleus.

25. IC 5063 (IRAS F20481−5715; AM2048−571): This is an S0/a (HyperLeda) considered as a merger remnant (Colina et al. 1991) and classified as a Seyfert 2. It shows high polarization in the near IR continuum (Hough et al. 1987) and strong broad Hα emission in polarized flux (Inglis et al. 1993). These results suggest that there is an obscured hidden broad-line region (HBLR) (e.g., Tran 2001; Lumsden et al. 2001; Antonucci & Miller 1985) and the broad emission line is scattered into our line of sight by scatters outside the obscured regions (Morganti et al. 2007). Also, this object is the first galaxy where a fast gas outflow has been discovered (Morganti et al. 1998). A Paα emission is strongly concentrated at the center and extended towards NW-SE direction, which may consistent with the direction of extend NLR reported by Colina et al. (1991).

26. ESO 286-G035 (IRAS F21008−4347): This is a spiral (Sc; HyperLeda) classified as an HII galaxy (Veilleux et al. 1995). In the Paα image, there is a strong emission line region at the center extended along the disk.

27. ESO 343-IG013 (IRAS F21330−3846; VV 714; AM 2133−384): This is a barred spiral (Sbc; HyperLeda) classed as an HII galaxy (Yuan et al. 2010; Veilleux et al. 1995). It is known as a strongly interacting pair (Vorontsov-Vel'Yaminov & Arkhipova 1974) with a separation between the two galactic nuclei of 10.″9 in the K_s-band image. The northern part of the galaxy has concentrated Paα emission at its center, while the southern part has strong Paα emission at the its center and extended region along spiral arms.

28. NGC 7130 (IRAS F21453−3511; AM 2145−351; NED 02): This is a spiral (Sc; HyperLeda) classified as LINER/Seyfert 1 (Corbett et al. 2003; Veilleux et al. 1995). It is known as a peculiar/disturbed spiral (Lauberts 1982) and a starburst/AGN composite galaxy (Levenson et al. 2005). In the Paα image, strong emission exists at the central region, as well as along the spiral arms, especially at the northern arm which is consistent with an Hα image (Rodríguez-Zaurín et al. 2011), and a Paα image by *HST*/NICMOS (Alonso-Herrero et al. 2006).

29. IC 5179 (IRAS F22132−3705; AM 2213−370): This is a barred spiral (Sbc; HyperLeda) classified as an HII galaxy (Yuan et al. 2010). Type Ia SN 1999ee and the Type Ib/c SN 1999ex have been discovered in this galaxy (Stritzinger et al. 2002). Paα emission is distributed along the spiral arms as clumpy knots. These HII knots, which are widely spread over the entire galaxy, is not be covered by the field of view of VLT/VIMOS (Rodríguez-Zaurín et al. 2011) and *HST*/NICMOS (Alonso-Herrero et al. 2006) observations.

30. ESO 534-G009 (IRAS F22359−2606): This is a spiral (Sab; HyperLeda) classified as a LINER (Veilleux et al. 1995). There is a strong Paα emission at the central region.

31. NGC 7469 (IRAS F23007+0836; Arp 298; NED 01; Mrk 1514; KPG 575A): This is a spiral (Sa; HyperLeda) classified as a Seyfert 1 (Veilleux et al. 1995). It is known to have a circumnuclear ring with a diameter on scales of 1.″5–2.″5 (Davies et al. 2004), which is observed in the radio (Wilson et al. 1991; Condon et al. 1991; Colina et al. 2001), in the optical (Mauder et al. 1994), in the mid-infrared (Miles et al. 1994; Soifer et al. 2003), and in the near-infrared (Genzel et al. 1995; Lai et al. 1999; Scoville et al. 2000) wavelengths. In Paα image, the ring structure can not be resolved by the seeing size of the ANIR data.

32. CGCG 453-062 (IRAS F23024+1916): This is a spiral (Sab; HyperLeda) classified as a LINER (de Vaucouleurs et al. 1991). In Paα image, it has extended

TABLE 3
Paα luminosities and derived star formation rates.

ID	Galaxy Name	Size(Paα) (kpc)	L(Paα) (ergs s^{-1})	SFR(Paα) ($M_\odot$ yr^{-1})	SFR(Paα)$_{\rm corr}$ ($M_\odot$ yr^{-1})	SFR(IR) ($M_\odot$ yr^{-1})	$E(B-V)$	Ref.
(1)	(2)	(3)	(4)	(5)	(6)	(7)	(8)	(9)
1	NGC 23	1.9	1.17×10^{41}	7.5	11.2	14.5	0.74	1
2	NGC 34	1.1	3.30×10^{41}	21.1	65.0	35.4	2.08	1
3	NGC 232	0.9	7.98×10^{40}	5.1	10.4	26.5	1.31	1
4	IC 1623A/B	9.8	6.02×10^{41}	38.5	44.3	58.9	0.26	1
5	ESO 244-G012	1.8	4.33×10^{41}	27.7	59.3	32.6	1.41	3
6	UGC 2238	3.3	3.88×10^{41}	24.8	83.8	23.0	2.25	1
7	IRAS F02437+2122	0.5	2.46×10^{40}	1.6	5.0	17.6	2.13	1
8	UGC 2982	4.7	2.67×10^{41}	17.1	47.5	17.0	1.89	1
9	NGC 1614	1.1	5.97×10^{41}	38.2	74.7	49.0	1.24	1,2,3
10	MCG −05-12-006	0.8	1.28×10^{41}	8.2	[14.5]	15.8	[1.05]	–
11	NGC 1720	0.9	3.32×10^{40}	2.1	[3.8]	8.5	[1.05]	–
12	ESO 557-G002	1.2	9.02×10^{40}	5.8	7.3	18.6	0.43	2,3
13	IRAS F06592-6313	0.7	7.39×10^{40}	4.7	9.4	17.0	1.28	3
14	NGC 2342	10.9	1.55×10^{41}	9.9	[17.5]	27.0	[1.05]	–
15	ESO 320-G030	1.5	4.26×10^{40}	2.7	5.1	20.3	1.16	3
16	NGC 4922	1.2	5.50×10^{40}	3.5	[6.2]	22.7	[1.05]	–
17	MCG −03-34-064	0.3	7.45×10^{40}	4.8	[8.4]	20.4	[1.05]	–
18	NGC 5135	1.4	1.72×10^{41}	11.0	14.2	20.0	0.46	3
19	NGC 5257/8	9.5/10.6	$2.65\times10^{41}/1.93\times10^{41}$	16.9/12.4	20.8/15.2	37.5	0.38	1,2
20	IC 4518A/B	0.7/4.6	$4.51\times10^{+40}/2.86\times10^{40}$	2.9/1.8	3.7/2.3	13.4	0.43	2,3
21	IC 4686/87	0.6/2.5	$8.81\times10^{40}/5.41\times10^{41}$	5.6/34.6	8.2/45.6	38.2	0.69	2,3
21c	IC 4689	2.2	1.42×10^{41}	9.1	16.0	–	[1.05]	-
22	IRAS F18293-3413	1.8	6.29×10^{41}	40.3	104.3	70.6	1.76	1
23	ESO 339-G011	1.3	7.37×10^{40}	4.7	[8.3]	14.8	[1.05]	–
24	NGC 6926	24.5	1.16×10^{41}	7.4	14.3	22.2	1.22	1,2
25	IC 5063	0.8	2.64×10^{40}	1.7	[3.0]	7.8	[1.05]	–
26	ESO 286-G035	2.1	1.76×10^{41}	11.3	[19.9]	19.0	[1.05]	–
27	ESO 343-IG013	1.6	7.09×10^{40}	4.5	7.5	13.7	0.93	1,2
28	NGC 7130	1.0	1.35×10^{41}	8.6	14.2	26.5	0.92	1,2,3
29	IC 5179	5.4	1.62×10^{41}	10.4	19.0	17.5	1.11	1,3
30	ESO 534-G009	0.5	6.53×10^{39}	0.4	0.6	5.4	0.63	1
31	NGC 7469	1.0	3.71×10^{41}	23.7	23.7	50.0	0.00	1
32	CGCG 453-062	4.1	1.23×10^{41}	7.9	[13.9]	27.7	[1.05]	–
33	NGC 7591	5.4	6.79×10^{40}	4.3	9.2	13.9	1.39	1
34	NGC 7678	18.8	3.41×10^{40}	2.2	[3.8]	7.4	[1.05]	–
35	MCG −01-60-022	1.3	1.61×10^{41}	10.3	21.9	20.9	1.40	2
36	NGC 7770/1	2.3/3.4	$8.75\times10^{40}/1.77\times10^{+41}$	5.6/11.3	7.8/34.0	28.6	2.03	1
37	Mrk 331	1.6	2.14×10^{41}	13.7	[24.2]	32.4	[1.05]	–
38	UGC 12914/15	6.8/12.2	$6.34\times10^{40}/3.85\times10^{40}$	4.1/2.5	[7.2]/[4.4]	10.5	[1.05]	–

Note. — Column (1): Galaxy ID in this paper. Column (2): Galaxy name. Column (3): Size of Paα emission line regions in diameter defined to be an elliptical (major axis) contained 50% flux within the Petrosian radius (Peterson et al. 2012). Column (4): Observed Paα luminosities. Column (5): Paα-derived star formation rates. Column (6): Paα-derived star formation rates with dust extinction correction. Brackets values are dust-extinction corrected SFRs by using assumed $E(B-V)=1.05$, the average value of all our objects. Column (7): IR-drived star formation rates. Column (8): Amount of dust extinction derived from balmer decrement using the flux ratio of Hα and Hβ. Column (9): References for the dust extinction. 1; Veilleux et al. (1995), 2; Dopita et al. (2002), 3; Rodríguez-Zaurín et al. (2011)

star-forming region distributed not only at the central region but also along the disk.

33. NGC 7591 (IRAS F23157+0618): This is an isolated (Yuan et al. 2010) barred spiral (SBbc; HyperLeda) classified as a LINER (Veilleux et al. 1995). In Paα image, a strong emission peak is at the central region, and diffuse emission regions distributed along the spiral arms and the barred structure.

34. NGC 7678 (IRAS F23259+2208; Arp 028; VV 359): This is a barred spiral (Sc; HyperLeda) classified as an HII galaxy (Ann & Kim 1996). It has a massive spiral arm in the southern part of the galaxy, and is considered to have experienced strong interaction which induced active star formation in the nucleus and in the southern arm (Ann & Kim 1996). In Paα image, strong emission line regions are at the central region, and at the southern arm. Extended diffuse emission can be seen along the spiral arms.

35. MCG −01-60-022 (IRAS F23394−0353; VV 034a; Arp 295B): This is a merging spiral (Sb; HyperLeda) classified as an HII galaxy (Corbett et al. 2003). It is known as an interacting galaxy (Vorontsov-Vel'Yaminov & Arkhipova 1974; Roche 2007) paired with MCG −01-60-021, separated by 4′.5 in the $K_{\rm s}$-band image. In Paα image, a strong emission is detected not only at the central region but also along the disk, while a Paα emission can not be detected in the tidal tail between Arp 295A and Arp 295B.

36. NGC 7770/1 (IRAS F23488+19489; Mrk 9006; KPG 592B): This appears to be in the early stage of an interaction with NGC 7770 where a separation between the two galactic nuclei is 1′ in the $K_{\rm s}$-band

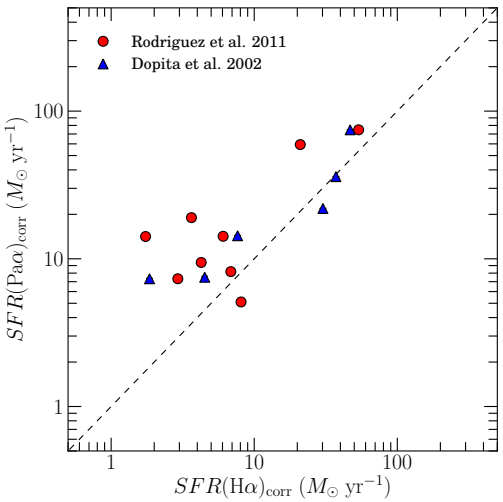

FIG. 4.— Comparison of SFRs derived from Hα and Paα luminosities, both corrected for dust extinction. Hα luminosities are taken from Rodríguez-Zaurín et al. (2011) (circles) and Dopita et al. (2002) (triangles). The dashed line shows the one-to-one relation.

image. NGC 7770 is a spiral (S0-a; HyperLeda), and NGC 7771 is a barred spiral (Sa; HyperLeda) classified as an HII galaxy (Veilleux et al. 1995). Both NGC 7771 and NGC 7770 show a strong Paα emission. NGC 7770 has strong emission in the spiral arm rather than at the central region, while NGC 7771 has strong emission at the central region rather than in the disk. The morphology of central Paα emission in NGC 7771 seems to be a ring starburst. No Paα emission is detected between these galaxies.

37. Mrk 331 (IRAS F23488+1949; KPG 593B): This is a member of a group of three galaxies; an irregular separated by 1.′4 and a spiral by 2′ (Mirabel 1983). It is a spiral (Sa; HyperLeda) classified as an HII/Seyfert 2 (Soifer et al. 2001). In Paα image, an emission line appears to be concentrated at the central region.

38. UGC 12914/5 (IRAS F23591+2312; VV 254; III Zw 125; KPG 603; TaffyI): These are barred galaxies (SBc; HyperLeda). It is an interacting system with an extended shock-induced synchrotron radio emission connecting the two galaxies (Condon et al. 1993; Peterson et al. 2012). The steepening of the radio spectral index at the bridge indicates a face-on collision which occurred only 20 Myr ago (Condon et al. 1993). There are many HII blobs in a Paα image, and it is considered that many of them are induced by the collision (Komugi et al. 2012).

5. DISCUSSION

5.1. *The Effect of Dust-extinction for Paα Flux*

Even though the Paα emission line is less sensitive against dust extinction, we can not ignore its effect. Typical amount of dust extinction in LIRGs is $A_V \sim 4$ mag (Alonso-Herrero et al. 2006) as derived by the "Balmer Decrement Method" (Calzetti et al. 2000) using the flux ratio of Hα and Paα. To correct for the dust-extinction in our sample, we adopt the extinction curve of Calzetti et al. (2000) with $R_V = 4.05$, which results in $A_V/A_{\mathrm{Pa}\alpha} = 6.97$, and $A_{\mathrm{H}\alpha}/A_{\mathrm{Pa}\alpha} = 5.68$, meaning that Pa$\alpha$ is typically attenuated by 0.57 mag in LIRGs. In Table 3, color excess ($E(B-V)$) derived by balmer decrement method using ratios of Hα and Hβ taken from Veilleux et al. (1995), Dopita et al. (2002), and Rodríguez-Zaurín et al. (2011) are listed. 26 galaxies, with Hα and Hβ data in our sample have $A_V = 4.25$ mag ($E(B-V) = 1.05$) on average, and we adopt this value for the rest of the sample.

5.2. *Star Formation Rates*

SFRs are derived from Paα luminosity using the following relation, assuming a relation on SFR-Hα luminosity assuming a Kroupa IMF (Kennicutt et al. 2009) and a flux ratio of Hα/Paα = 8.6 ($T = 1000$ K, $n_e = 10^4$ cm^{-3}, Hummer & Storey 1987) in starburst galaxies;

$$SFR(\mathrm{Pa}\alpha)(M_\odot\ \mathrm{yr}^{-1}) \equiv 6.4 \times 10^{-41} L(\mathrm{Pa}\alpha)(\mathrm{erg\ s}^{-1}) \quad (4)$$

where L(Paα) is the luminosity of Paα. Dust-extinction uncorrected star formation rates (SFR(Paα)) obtained from L(Paα) and those corrected for dust-extinction ($SFR(\mathrm{Pa}\alpha)_{\mathrm{corr}}$) are shown in Table 3.

Figure 4 shows the comparision between $SFR(\mathrm{Pa}\alpha)_{\mathrm{corr}}$ and SFR derived from the dust-extinction corrected Hα luminosity ($SFR(\mathrm{H}\alpha)_{\mathrm{corr}}$). The dust-extinction corrected Hα luminosities are taken from Rodríguez-Zaurín et al. (2011) and Dopita et al. (2002), which are obtained by narrow-band imaging or integral field spectroscopy. Their correlation is generally good, but $SFR(\mathrm{Pa}\alpha)_{\mathrm{corr}}$ is larger than $SFR(\mathrm{H}\alpha)_{\mathrm{corr}}$ systematically, while both are expected to be the same value because it is emitted from a same region by a same mechanism. Liu et al. (2013b) have found that correcting dust extinction using Hα/Paβ gives much larger star formation rate than using Hα/Hβ (Balmer decrement) in star formation regions of M83. Considering this study, the difference between $SFR(\mathrm{Pa}\alpha)_{\mathrm{corr}}$ and $SFR(\mathrm{H}\alpha)_{\mathrm{corr}}$ suggests that Paα can see star-forming activity through a more dusty region than Hα.

FIR and bolometric infrared luminosities are also good indicators for star formation in dusty starburst galaxies (e.g., Kennicutt 1998; Kewley et al. 2002; Hirashita et al. 2003), because MIR to FIR emission in these galaxies arises from re-radiation of dust-absorbed shorter-wavelength photons. Bolometric IR luminosities (L(IR)) are derived from the *IRAS* ADDSCAN/SCANPI 12 μm, 25 μm, 60 μm, and 100 μm data (Rush et al. 1993; Sanders et al. 2003) compiled by Sanders et al. (2003) and the following relation (Sanders & Mirabel 1996);

$$L(\mathrm{IR}) = 4\pi D_L^2 \times (1.8 \times 10^{-14}(13.48 f_{12} + 5.16 f_{25} + 2.58 f_{60} + f_{100})), \quad (5)$$

where D_L is the luminosity distance in meters, and f_{12}, f_{25}, f_{60}, and f_{100} are the IRAS flux densities in Jy at 12, 25, 60, and 100 μm, respectively. Then, SFR(IR) is derived using the following relation (Calzetti 2013);

$$SFR(\mathrm{IR})\ (M_\odot\ \mathrm{yr}^{-1}) \equiv 2.8 \times 10^{-44}\ L(\mathrm{IR})\ (\mathrm{erg\ s}^{-1}), \quad (6)$$

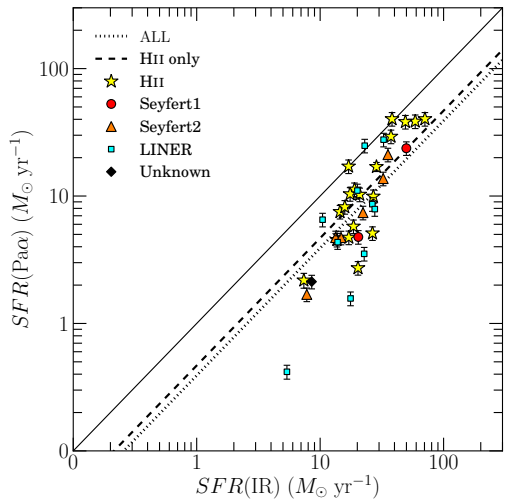

FIG. 5.— Comparison of SFRs derived from bolometric infrared luminosities calculated using *IRAS* ADDSCAN FIR luminosities of 12 μm, 25 μm, 60 μm, and 100 μm, and those derived from Paα luminosities. The dotted line represents the best fit relation for all galaxies assuming a slope of one while the dashed line represents for the HII galaxies. The solid line shows the one-to-one relation. Stars represent HII galaxies, circles Seyfert Is, triangles Seyfert IIs, squares LINERs, and diamonds galaxies without any classification. The error bars are the total uncertainties on the measurement of the Paα flux ($\sigma_{\rm total}$; see text).

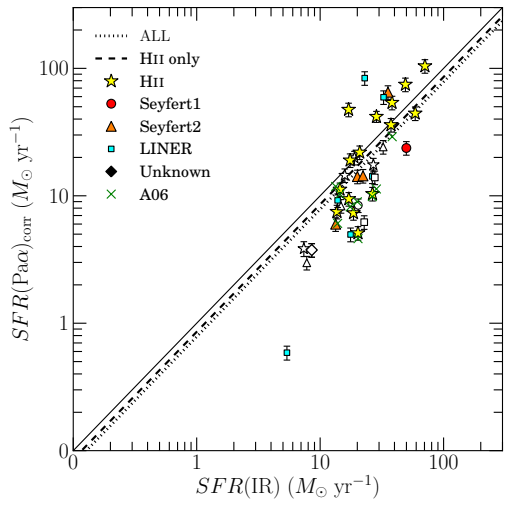

FIG. 6.— Same as Figure 5, but plot for SFRs derived from dust-extinction corrected Paα luminosities. Filled symbols represent galaxies whose extinction is corrected using Balmer decrement method while open symbols assuming $E(B-V)$=1.05. Crosses show galaxies whose Paα data are observed by *HST*/NICMOS and its extinction is corrected using Balmer decrement method (Alonso-Herrero et al. 2006, A06). The error bars are the total uncertainties on the measurement of the Paα flux ($\sigma_{\rm total}$; see text).

The results are listed in Table 3.

Comparison of SFR(IR) and SFR(Paα) is shown in Figure 5. The solid line shows the one-to-one relation between SFR(IR) and SFR(Paα). The dotted line represents the best fit relation for all galaxies assuming a slope of one and the dashed line represents the same but using only HII galaxies. Both indicate that SFR(Paα) are systematically offset by -0.3 dex from SFR(IR).

Figure 6 is comparison of SFR(IR) and $SFR(\mathrm{Pa}\alpha)_{\rm corr}$. Some samples have no H$\alpha$ data, therefore we correct for dust-extinction assuming $E(B-V)=1.05$ ($A_V=4.3$) which is an average value of our sample. In this figure, we also plot a sample of galaxies from Alonso-Herrero et al. (2006) where SFR(Paα) are derived in the same way as described above, but we do not use this sample in our best-fitting relations. The offset between $SFR(\mathrm{Pa}\alpha)_{\rm corr}$ and SFR(IR) is -0.07 dex within a scatter for 0.27 dex.

5.2.1. *Malmquist Bias*

In Figure 5 and 6, it seems that the slopes of the distribution of HII galaxies are larger than that of one. Actually, the slopes are 1.8 in Figure 5 and 2.1 in Figure 6. This may be caused by "Malmquist bias" (Malmquist 1925), where brightness of a sample falls off quickly until the brightness falls below observational threshold, because the luminosity range of our sample is spread over only 1 order of magnitude. Therefore we have estimated this effect in our sample with the following a simple test.

We first create a model set of 38 galaxies with SFR of "X" ($M_\odot$ yr^{-1}) within the same IR luminosity range as our sample. This X for each galaxy is converted into "Y" by adding Gaussian-random "noise" with $\sigma=0.3$ dex, which is the same value as the dispersion between $\log(SFR(\mathrm{Pa}\alpha)_{\rm corr})$ and $\log(SFR(\mathrm{IR}))$. Then, a best-fit relation is obtained for the plot of X and Y. In this fitting, two kinds of relations are used; one is 1 free-parameter function ($\log(Y)=\log(X)+b$) and the other is two free-parameters function ($\log(Y)=a\cdot\log(X)+b$). We have carried out the above procedure 1000 times.

In the 2 free-parameter fitting, we find the slope a to be 2.0 ± 0.3, which is larger than the intrinsic value of 1 and consistent with the observed value of $a=2.1$. In the 1 free-parameter fitting, we find that the offset is $b=0\pm0.05$. The Large slope of the distributions in Figure 5 and in Figure 6 come from the Malmquist bias. To remove the Malmquist bias it is necessary to expand the luminosity range. The offset of -0.07 dex in Figure 6 with 1 free-paramter fitting is within the statistical error.

5.2.2. *Comparison Between IR SFR and Paα SFR*

From our simple test, the vertical offsets in Figure 5 and in Figure 6 are insensitive to the Malmquist bias. To explain the offset of -0.3 dex in Figure 5 by dust-extinction, $A_V=5.7$ is required. Alonso-Herrero et al. (2006) suggested that the spectroscopic dust-extinction derived from an Hα and Paα is $A_V=4.1$ on average, which is almost the same value as our result but slightly smaller. Figure 6 shows that there is a relatively good coincidence between the $SFR(\mathrm{Pa}\alpha)_{\rm corr}$ and the SFR(IR) on average.

Although our result shows that there is a good correlation between $SFR(\mathrm{Pa}\alpha)_{\rm corr}$ and SFR(IR), some of the galaxies have offset from it. For example, ESO 534-G009, having lowest $SFR(\mathrm{Pa}\alpha)_{\rm corr}$ in our sample, is a late-type spiral (Sab) classified as a LINER, and its Paα emission is emitted from a unresolved compact central region. This galaxy shows an order of magnitude lower $SFR(\mathrm{Pa}\alpha)_{\rm corr}$ than SFR(IR). The galaxies with smaller $SFR(\mathrm{Pa}\alpha)_{\rm corr}$ than SFR(IR) may have larger

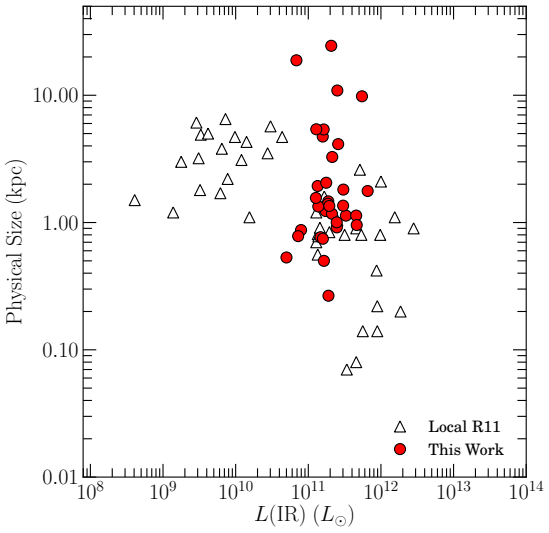

FIG. 7.— Comparison of $L(\mathrm{IR})$ and physical sizes (in diameter) of star-forming regions. To compare with local sample in R11, the area of star-forming region is measured in Paα images convolved with a gaussian function with $\sigma = 4$ kpc in physical scale. Triangles represent normal galaxies and U/LIRGs derived from R11.

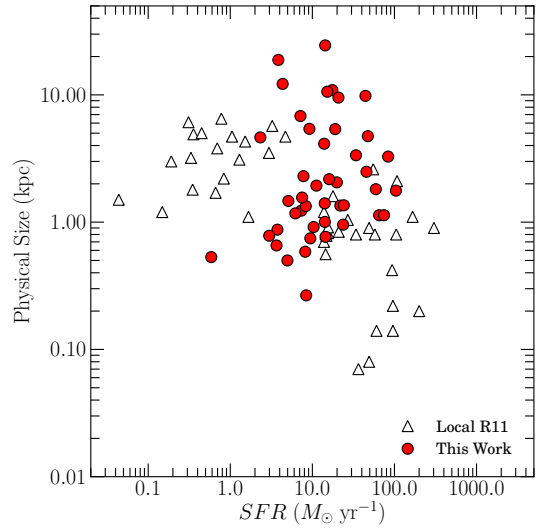

FIG. 8.— Comparison of SFR and physical sizes (in diameter) of star-forming regions. Same as Figure 7, the area of star-forming region is measured in Paα images with being convolved. SFRs are derived not only from Paα but also from MIR luminosity in R11.

dust extinction than measured; indeed, Piqueras López et al. (2013) shows that dust-extinction of central region of LIRGs are estimated to be $A_V = 5 \sim 13$ mag by using infrared indicators, larger than the value obtained using optical. Another possibility is contribution to IR luminosity by dust particles heated by more evolved stars, called the "IR cirrus" component (e.g., Kennicutt 1998; Kennicutt et al. 2009), which may overestimate $SFR(\mathrm{IR})$.

5.3. *Surface Densities of IR Luminosity and Star Formation Rate*

The size of star-forming regions in LIRGs at high IR luminosity end and in ULIRGs are compact while the normal galaxies show extended star-forming region over a few kilo-parsecs along the spiral arm (e.g., Soifer et al. 2000; Díaz-Santos et al. 2010; Alonso-Herrero et al. 2012). R11 find that the size of star-forming regions changes drastically at the LIRG luminosity, suggesting that these differences are caused by strong interaction (Totani et al. 2011). However, there are few sample at the "transition" point. To investigate this relationship between the size and star-forming activity, we measure sizes of star-forming regions in our large sample of LIRGs with Paα emission line images, which fill the gap between normal galaxies and ULIRGs in R11.

We define size of a star-forming region of a galaxy to be an elliptical diameter (major axis) containing 50% flux within a Petrosian radius (Petrosian 1976) defined in the Paα line image convolved with a Gaussian function with $\sigma = 4$ kpc in physical scale as done in R11 and list it in column-(3) of Table 3. Figure 7 shows the comparison between the IR luminosities and the sizes of the star-forming regions except for the 5 galaxies (NGC 5257/8, IC 4518A/B, IC 4686/7, NGC 7770/1, UGC 12914/5) which are paired galaxies and the size of SFR can not be defined. We find that the sizes of the LIRGs in our sample is distributed from 0.3 kpc or less to 25 kpc. Especially, IC 1623A/B, NGC 2342, NGC 7678, NGC 6926 have a large (> 9.5 kpc) star-forming regions along their spiral arms. Figure 8 shows the comparison between the SFRs derived from Paα and the sizes of the star-forming regions including 5 galaxies (NGC 5257/8, IC 4518A/B, IC 4686/7, NGC 7770/1, UGC 12914/5) removed from Figure 7. Our results fill the blank parameter space between normal galaxies and ULIRGs in R11.

Figure 9 shows a comparison of IR luminosites and surface densities of IR luminosity ($\Sigma_{L(\mathrm{IR})}$) derived by dividing a IR by area of a star-forming region;

$$\Sigma_{L(\mathrm{IR})} \equiv L(\mathrm{IR})/(\pi r_m^2), \quad (7)$$

where r_m is the Petrosian radius listed in Table 3. In this figure, the dotted line represents the sequence of normal galaxies derived by best fitting of local normal galaxies and high-z star-forming galaxies in R11 and Rujopakarn et al. (2013). R11 shows that the sequence of local U/LIRGs is different from that of local normal galaxies. Therefore we obtained the sequence of U/LIRGs by fitting sub-LIRGs ($L(\mathrm{IR}) \geq 10^{10}\ L_\odot$) and ULIRGs of both ours and those in R11 with the dashed line, that is $\log_{10}(\Sigma_{L(\mathrm{IR})}) = 3.6 \times \log_{10}(L(\mathrm{IR})) - 30.0$.

Figure 7 and 9 show that $\Sigma_{L(\mathrm{IR})}$ become higher and the size of the star-forming region become more compact as the $L(\mathrm{IR})$ increase, and the transition point from the sequence of normal galaxies and U/LIRGs is at $L(\mathrm{IR}) = 8 \times 10^{10}\ L_\odot$, which is consistent with the result of R11.

Figure 10 shows a comparison of SFRs derived from Paα and surface densities of SFR (Σ_{SFR}) derived by dividing a SFR by area of a star-forming region;

$$\Sigma_{SFR} \equiv \mathrm{SFR}/(\pi r_m^2). \quad (8)$$

The dashed line is the best fit linear relation for U/LIRGs and sub-LIRGs ($SFR \geq 1.1\ M_\odot\ \mathrm{yr}^{-1}$) including both ours and those in R11, where $\log_{10}(\Sigma_{\mathrm{SFR}}) = 3.4 \times \log_{10}(\mathrm{SFR}) - 3.2$. In this plot, our results fill the blank

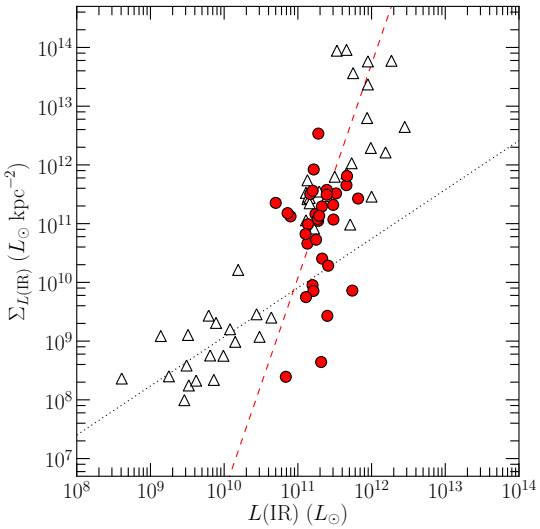

FIG. 9.— Comparison of L(IR) and L(IR) surface densities. The dotted line represent the sequence of normal galaxies (R11), while dashed line the sequence of U/LIRGs, which is the best fit relation using the sample from this work and R11.

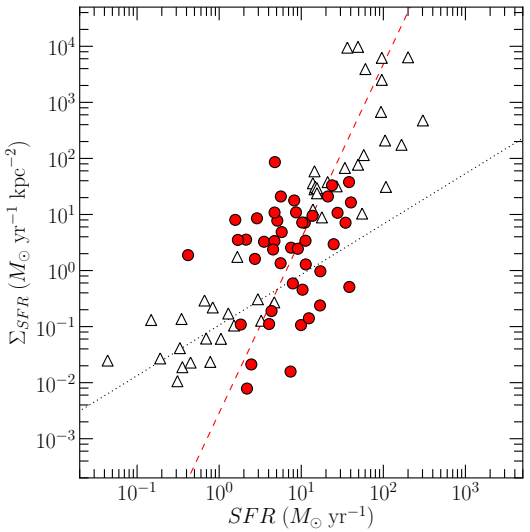

FIG. 10.— Comparison of SFRs derived from Paα luminosities and SFR surface densities. The dotted line represent the sequence of normal galaxies (R11; Rujopakarn et al. 2013), while dashed line the sequence of U/LIRGs, which is the best fit relation using the sample from this work and R11.

between the sequence of normal galaxies and U/LIRGs, and the transition point is at $SFR = 7\ M_\odot\ \mathrm{yr}^{-1}$, which is a consistent value with that in the $\Sigma_{L(\mathrm{IR})}$–L(IR) relation.

Also we find that there is a large scatter in both figures, different from those of normal galaxies and U/LIRGs in R11. Some simulations of galaxy formation suggest that while merging or interacting galaxies in their early stages have extended star-forming regions along their collision interfaces and disks (Saitoh et al. 2009), late-stage mergers have compact and concentrated star-forming regions at their centers (Barnes & Hernquist 1996). Our results show that while LIRGs have a wide range in sizes of the star-forming regions from less than 1 kpc to over 10 kpc, almost all LIRGs at high luminosity end and ULIRGs have compact star-forming region around 1 kpc or less. Considering the fact that all the ULIRGs are mergers (Soifer et al. 2000), there is a possibility that ULIRGs and LIRGs at high luminosity end with compact star-forming regions are at the late-stage in the merging history. On the other hand, from sub-LIRGs and LIRGs at low luminosity end with extended star-forming regions may be at first-stage in merging history.

6. SUMMARY

We have observed 38 galaxy system listed in *IRAS* RBGS catalog in Paα with narrow-band imaging (cz = 2800–8100 km s^{-1}, L(IR) = 4.5×10^{10}–6.5×10^{11} $L_\odot$) using near infrared camera (ANIR) for the University of Tokyo Atacama Observatory 1m telescope, installed at the summit of Co. Chajnantor in northern Chile.

We have estimated the Paα fluxes from the narrow-band images with our newly developed flux calibration method. We find that $SFR(\mathrm{Pa}\alpha)_{\mathrm{corr}}$ which is SFR obtained from Paα luminosity corrected for the effect of dust extinction with balmer decrement method (Hβ/Hα) shows good agreement with SFR(IR), which is star formation estimated from total infrared luminoisity. This result suggests that Paα with dust-correction is sufficient for estimating SFR of whole the galaxy. However, some galaxies have large differences between the $SFR(\mathrm{Pa}\alpha)_{\mathrm{corr}}$ and the SFR(IR), which may be caused by effect of AGNs, strong dust-extinction, or IR cirrus component.

We also obtain surface densities of L(IR) ($\Sigma_{L(\mathrm{IR})}$) and SFR (Σ_{SFR}) for individual galaxies by measuring physical sizes of star-forming regions. The range of SFR in our sample (from 0.6 to $\sim$ 104 $M_\odot$ yr^{-1}) fill the blank of the range of SFR in the previous work. We find that most of the samples follow a sequence of local U/LIRGs on the L(IR)-$\Sigma_{L(\mathrm{IR})}$ and SFR-Σ_{SFR} plane. We confirm that a transition of the sequence from normal galaxies to U/LIRGs is seen at $L(\mathrm{IR}) = 8 \times 10^{10}$. Also, we find that there is a large scatter in physical size, different from those of normal galaxies or ULIRGs. Considering the fact that most of U/LIRGs are merging or interacting galaxies, these scatters may be caused by the strong external factors or the differences of their merging stage.

We deeply thank the referee (Dr. Guilin Liu) for useful comments and suggestions that helped improve the quality of the paper, and we also thank M. Malkan (UCLA) and S. Howard (CfA) for enlightening discussions on this topic. This work is supported by Ministry of Education, Culture, Sports, Science and Technology of Japan, Grant-in-Aid for Scientific Research (17104002, 20040003, 20041003, 21018003, 21018005, 21684006, 22253002, 22540258,and 23540261) from the Japan Society for the Promotion of Science (JSPS). Operation of ANIR on the miniTAO 1m telescope is also supported by NAOJ Research Grant for Universities and Optical & Near-Infrared Astronomy Inter-University Cooperation Program, supported by the MEXT of Japan. Part of this work has been supported by the Institutional Program for Young Researcher Overseas Visits operated by JSPS. The Image Reduction and Analysis Facility (IRAF) used in this paper is distributed by the National Optical Astronomy Observatories, which are operated by

the Association of Universities for Research in Astronomy, Inc., under cooperative agreement with the National Science Foundation. We acknowledge the usage of the HyperLeda database (http://leda.univ-lyon1.fr).

REFERENCES

Alonso-Herrero, A., Ward, M. J., Aragon-Salamanca, A.,& Zamorano, J. 1999, MNRAS, 302, 561
Alonso-Herrero, A., Engelbracht, C. W., Rieke, M. J., Rieke, G. H., & Quillen, A. C. 2001, ApJ, 546, 952
Alonso-Herrero, A., Rieke, G. H., Rieke, M. J., & Scoville, N. Z. 2002, AJ, 124, 166
Alonso-Herrero, A., Rieke, G. H., Rieke, M. J., et al. 2006, ApJ, 650, 835
Alonso-Herrero, A., García-Marín, M., Monreal-Ibero, A., et al. 2009, A&A, 506, 1541
Alonso-Herrero, A., Pereira-Santaella, M., Rieke, G. H., & Rigopoulou, D. 2012, ApJ, 744, 2
Ann, H.-B., & Kim, J.-M. 1996, Journal of Korean Astronomical Society, 29, 255
Antonucci, R. R. J., & Miller, J. S. 1985, ApJ, 297, 621
Agüero, E. L., Paolantonio, S., Günthardt, G. 2000, AJ, 119, 94
Barnes, J. E., & Hernquist, L. 1996, ApJ, 471, 115
Calzetti, D., Armus, L., Bohlin, R. C., et al. 2000, ApJ, 533, 682
Calzetti, D., Kennicutt, R. C., Engelbracht, C. W., et al. 2007, ApJ, 666, 870
Calzetti, D., 2013, arXiv:1208.2997v1, in press
Cardelli, J. A., Clayton, G. C., & Mathis, J. S. 1989, ApJ, 345, 245
Caputi, K. I., Lagache, G., Yan, L., et al. 2007, ApJ, 660, 97
Chaboyer, B., & Vader, J. P. 1991, PASP, 103, 35
Colina, L., Alberdi, A., Torrelles, J. M., Panagia, N., & Wilson, A. S. 2001, ApJ, 553, L19
Colina, L., Sparks, W. B., & Macchetto, F. 1991, ApJ, 370, 102
Condon, J. J., Huang, Z.-P., Yin, Q. F., & Thuan, T. X. 1991, ApJ, 378, 65
Condon, J. J., Helou, G., Sanders, D. B., & Soifer, B. T. 1993, AJ, 105, 1730
Corbett, E. A., Kewley, L., Appleton, P. N., et al. 2003, ApJ, 583, 670
Daddi, E., Elbaz, D., Walter, F., et al. 2010, ApJ, 714, L118
Davies, R. I., Tacconi, L. J., & Genzel, R. 2004, ApJ, 602, 148
de Vaucouleurs, G., de Vaucouleurs, A., Corwin, H. G., Jr., et al. 1991, S&T, 82, 621
Díaz-Santos, T., Charmandaris, V., Armus, L., et al. 2010, ApJ, 723, 993
Dopita, M. A., Pereira, M., Kewley, L. J., & Capaccioli, M. 2002, ApJS, 143, 47
Falcke, H., Rieke, M. J., Rieke, G. H., Simpson, C., & Wilson, A. S. 1998, ApJ, 494, L155
Fernández, X., van Gorkom, J. H., Schweizer, F., & Barnes, J. E. 2010, AJ, 140, 1965
Genzel, R., Weitzel, L., Tacconi-Garman, L. E., et al. 1995, ApJ, 444, 129
Goto, T., Takagi, T., Matsuhara, H., et al. 2010, A&A, 514, A6
Grimes, J. P., Heckman, T., Hoopes, C., et al. 2006, ApJ, 648, 310
Hill, G. J., Goodrich, R. W., & Depoy, D. L. 1996, ApJ, 462, 163
Hirashita, H., Buat, V., & Inoue, A. K. 2003, A&A, 410, 83
Hough, J. H., Brindle, C., Axon, D. J., Bailey, J., & Sparks, W. B. 1987, MNRAS, 224, 1013
Ho, L. C., Filippenko, A. V., & Sargent, W. L. W. 1997, ApJS, 112, 315
Hopkins, A. M., & Beacom, J. F. 2006, ApJ, 651, 142
Hummer, D. G., & Storey, P. J. 1987, MNRAS, 224, 801
Inglis, M. D., Brindle, C., Hough, J. H., et al. 1993, MNRAS, 263, 895
Iono, D., Yun, M. S., & Ho, P. T. P. 2005, ApJS, 158, 1
Iono, D., Saito, T., Yun, M. S., et al. 2013, PASJ, 65, L7
Jenkins, L. P., Roberts, T. P., Ward, M. J., & Zezas, A. 2005, MNRAS, 357, 109
Kennicutt, R. C., Jr. 1998, ARA&A, 36, 189
Kennicutt, R. C., Jr., Calzetti, D., Walter, F., et al. 2007, ApJ, 671, 333
Kennicutt, R. C., Jr., Hao, C.-N., Calzetti, D., et al. 2009, ApJ, 703, 1672
Kewley, L. J., Geller, M. J., Jansen, R. A., & Dopita, M. A. 2002, AJ, 124, 3135
Kim, D.-C., Veilleux, S., & Sanders, D. B. 1998, ApJ, 508, 627
Kim, D., Im, M., & Kim, M. 2010, ApJ, 724, 386
Komugi, S., Sofue, Y., Nakanishi, H., Onodera, S., & Egusa, F. 2005, PASJ, 57, 733
Komugi, S., Tateuchi, K., Motohara, K., et al. 2012, ApJ, 757, 138
Konishi, M., Motohara, K., Tateuchi, K., et al. 2013, PASJ, accepted
Koss, M., Mushotzky, R., Baumgartner, W., et al. 2013, ApJ, 765, L26
Lada, C. J., Forbrich, J., Lombardi, M., & Alves, J. F. 2012, ApJ, 745, 190
Lai, O., Rouan, D., & Alloin, D. 1999, European Southern Observatory Conference and Workshop Proceedings, 56, 555
Lauberts, A. 1982, Garching: European Southern Observatory (ESO), 1982,
Levenson, N. A., Weaver, K. A., Heckman, T. M., Awaki, H., & Terashima, Y. 2005, ApJ, 618, 167
Liu, G., Calzetti, D., Kennicutt, R. C., Jr., et al. 2013, ApJ, 772, 27
Liu, G., Calzetti, D., Hong, S., et al. 2013, ApJ, 778, LL41
Lord, S. D. 1992, NASA Technical Memorandum, 103957
Lumsden, S. L., Heisler, C. A., Bailey, J. A., Hough, J. H., & Young, S. 2001, MNRAS, 327, 459
Lutz, D. 1991, Dynamics of Galaxies and Their Molecular Cloud Distributions, 146, 312
Malmquist, K. G. 1925, The Observatory, 48, 142
Mauder, W., Weigelt, G., Appenzeller, I., & Wagner, S. J. 1994, A&A, 285, 44
Miles, J. W., Houck, J. R., & Hayward, T. L. 1994, ApJ, 425, L37
Mirabel, I. F. 1983, ApJ, 270, L35
Minezaki, T., Kato, D., Sako, S., et al. 2010, Proc. SPIE, 7733,
Morganti, R., Oosterloo, T., & Tsvetanov, Z. 1998, AJ, 115, 915
Morganti, R., Holt, J., Saripalli, L., Oosterloo, T. A., & Tadhunter, C. N. 2007, A&A, 476, 735
Motohara, K., Aoki, T., Sako, S., et al. 2008, Proc. SPIE, 7012,
Motohara, K., Mitani, N., Sako, S., et al. 2008, Proc. SPIE, 7014,
Motohara, K., Konishi, M., Toshikawa, K., et al. 2010, Proc. SPIE, 7735,
Motohara, K. M., Aoki, T., Asano, K., et al. 2011, Revista Mexicana de Astronomia y Astrofisica Conference Series, 41, 83
Murphy, T. W., Jr., Soifer, B. T., Matthews, K., Kiger, J. R., & Armus, L. 1999, ApJ, 525, L85
Naim, A., Lahav, O., Buta, R. J., et al. 1995, MNRAS, 274, 1107
Olsson, E., Aalto, S., Thomasson, M., & Beswick, R. 2010, A&A, 513, A11
Paturel G., Petit C., Prugniel P., Theureau G., Rousseau J., Brouty M., Dubois P., Cambrésy L., 2003, A&A, 412, 45
Peterson, B. W., Appleton, P. N., Helou, G., et al. 2012, ApJ, 751, 11
Petrosian, V. 1976, ApJ, 209, L1
Rieke, G. H., Alonso-Herrero, A., Weiner, B. J., et al. 2009, ApJ, 692, 556
Piqueras López, J., Colina, L., Arribas, S., & Alonso-Herrero, A. 2013, arXiv:1304.0894
Richter, O.-G., Sackett, P. D., & Sparke, L. S. 1994, AJ, 107, 99
Roche, N. D. 2007, RMXAA, 43, 179
Rodríguez-Zaurín, J., Arribas, S., Monreal-Ibero, A., et al. 2011, A&A, 527, A60
Rothberg, B., & Joseph, R. D. 2004, AJ, 128, 2098
Rujopakarn, W., Eisenstein, D. J., Rieke, G. H., et al. 2010, ApJ, 718, 1171
Rujopakarn, W., Rieke, G. H., Eisenstein, D. J., & Juneau, S. 2011, ApJ, 726, 93 (R11)
Rujopakarn, W., Rieke, G. H., Weiner, B. J., et al. 2013, ApJ, 767, 73
Rush, B., Malkan, M. A., & Spinoglio, L. 1993, ApJS, 89, 1
Saito, T., Iono, D., Yun, M., et al. 2013, Astronomical Society of the Pacific Conference Series, 476, 287
Saitoh, T. R., Daisaka, H., Kokubo, E., et al. 2009, PASJ, 61, 481
Sanders, D. B., & Mirabel, I. F. 1996, ARA&A, 34, 749
Sanders, D. B., Mazzarella, J. M., Kim, D.-C., Surace, J. A., & Soifer, B. T. 2003, AJ, 126, 1607

Scoville, N. Z., Evans, A. S., Thompson, R., et al. 2000, AJ, 119, 991
Scoville, N. Z., Polletta, M., Ewald, S., et al. 2001, AJ, 122, 3017
Schweizer, F., & Seitzer, P. 2007, AJ, 133, 2132
Sheen, Y.-K., Jeong, H., Yi, S. K., et al. 2009, AJ, 138, 1911
Skrutskie, M. F., Cutri, R. M., Stiening, R., et al. 2006, AJ, 131, 1163
Stritzinger, M., Hamuy, M., Suntzeff, N. B., et al. 2002, AJ, 124, 2100
Spinoglio, L., Malkan, M. A., Rush, B., Carrasco, L., & Recillas-Cruz, E. 1995, ApJ, 453, 616
Spergel, D. N., Verde, L., Peiris, H. V., et al. 2003, ApJS, 148, 175
Soifer, B. T., Neugebauer, G., Matthews, K., et al. 2000, AJ, 119, 509
Soifer, B. T., Neugebauer, G., Matthews, K., et al. 2001, AJ, 122, 1213
Soifer, B. T., Bock, J. J., Marsh, K., et al. 2003, AJ, 126, 143
Tanabé, T., Motohara, K., Tateuchi, K., et al. 2013, PASJ, 65, 55
Tateuchi, K., Motohara, K., Konishi, M., et al. 2012a, Publication of Korean Astronomical Society, 27, 297
Tateuchi, K., Motohara, K., Konishi, M., et al. 2012b, Proc. SPIE, 8446,
Tateuchi, K., Motohara, K., Konishi, M., et al. 2013, Astronomical Society of the Pacific Conference Series, 476, 301
Thomas, H. C., Alexander, P., Clemens, M. S., et al. 2004, MNRAS, 351, 362
Totani, T., Takeuchi, T. T., Nagashima, M., Kobayashi, M. A. R., & Makiya, R. 2011, PASJ, 63, 1181
Tran, H. D. 2001, ApJ, 554, L19
van den Broek, A. C., van Driel, W., de Jong, T., et al. 1991, A&AS, 91, 61
Väisänen, P., Rajpaul, V., Zijlstra, A. A., Reunanen, J., & Kotilainen, J. 2012, MNRAS, 420, 2209
Veilleux, S., Kim, D.-C., Sanders, D. B., Mazzarella, J. M., & Soifer, B. T. 1995, ApJS, 98, 171
Véron-Cetty, M.-P., & Véron, P. 2006, A&A, 455, 773
Vorontsov-Vel'Yaminov, B. A., & Arkhipova, V. P. 1974, Morphological catalogue of galaxies., 5 (1974), 0
Wilson, A. S., Helfer, T. T., Haniff, C. A., & Ward, M. J. 1991, ApJ, 381, 79
West, R. M. 1976, A&A, 46, 327
Yoshii, Y., Aoki, T., Doi, M., et al. 2010, Proc. SPIE, 7733,
Yuan, T.-T., Kewley, L. J., & Sanders, D. B. 2010, ApJ, 709, 884

APPENDIX

DERIVATION OF PAα FLUX AFFECTED BY ATMOSPHERIC ABSORPTIONS

The TAO site is a suitable place for ground-based Paα observation thanks its low PWV. Still, there are many atmospheric absorption features within the wavelength range of the narrow-band filter (Figure 1) which vary temporally due to change of PWV, and it is difficult to obtain the emission-line flux accurately. We then estimate the intrinsic Paα flux as follows. Figure 11 represents a cartoon of a spectrum affected by the atmospheric absorption. The thin-solid curve represents the atmospheric transmittance, the dashed curve an intrinsic spectrum of a target, bold-solid an observed spectrum affected by the atmosphere, and the shaded areas the wavelength ranges of the H-, $N191$- and $K_{\rm s}$-band filters.

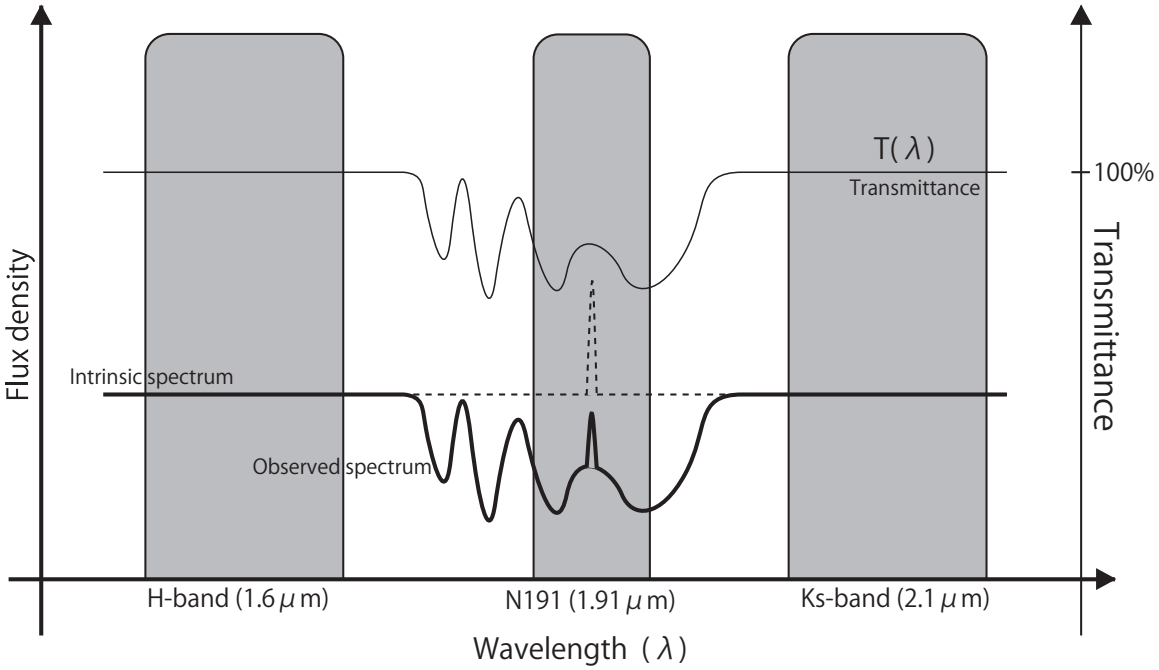

FIG. 11.— Cartoon of a model spectrum around the wavelength of Paα emission line, affected by the atmospheric absorption. H and $K_{\rm s}$ are the broad-band filters, and $N191$ is a narrow-band filter installed used for our observations. The thin curve represents the atmospheric transmittance, the dashed curve the intrinsic spectrum of the target, and the thick line the observed spectrum.

The intrinsic flux in the narrow-band filter ($F_{\rm int}^{N191}$) can be divided into two components; one is continuum ($F_{\rm int}^{c}$) and the other is emission line ($F_{\rm int}^{l}$). Then, the intrinsic flux can be written as

$$F_{\rm int}^{N191} = F_{\rm int}^{c} + F_{\rm int}^{l}. \tag{A1}$$

We also assume that the wavelength dependence of the continuum within the $N191$ filter is negligible. To derive $F_{\rm int}^{l}$ it is necessary to estimate the effect of instrumental absorption and atmospheric absorption due to PWV. The throughput ($\zeta_{\rm ANIR}$) can be written as

$$\zeta_{\rm ANIR} = T_{\rm Tel}^{N191} \times T_{\rm ANIR}^{N191} \times T_{\rm filter}^{N191} \tag{A2}$$

where $T_{\rm Tel}^{N191}$, $T_{\rm ANIR}^{N191}$, and $T_{\rm filter}^{N191}$ represent transmittance of the telescope, the instrument except the filter, and the N191 filter, described in K14. The atmospheric transmittance within the wavelength of the $N191$ narrow-band filter ($T_{\rm atm}^{{\rm PWV},N191})^X$) can be written as

$$(T_{\rm atm}^{{\rm PWV},N191})^X = \frac{\int_{\lambda_1}^{\lambda_2} T_{\rm atm}(\lambda) d\lambda}{\int_{\lambda_1}^{\lambda_2} d\lambda}, \tag{A3}$$

λ_1 and λ_2 represent cut-on and cut-off wavelength of the $N191$ narrow-band filter. Then the observed flux density of $N191$ can be written as follows,

$$F_{\rm obs}^{N191} = F_{\rm int}^{c} \zeta_{\rm ANIR} (T_{\rm atm}^{{\rm PWV},N191})^X + F_{\rm int}^{l} \zeta_{\rm ANIR} T_{\rm line} \tag{A4}$$

$$F_{\rm int}^{l} = \frac{1}{\zeta_{\rm ANIR} T_{\rm line}} (F_{\rm obs}^{N191} - F_{\rm int}^{c} \zeta_{\rm ANIR} (T_{\rm atm}^{{\rm PWV},N191})^X). \tag{A5}$$

In a narrow-band filter observation, an observed flux is the averaged flux of emission line within the wavelength range from λ_1 to λ_2, and the flux are calibrated by using the flux of 2MASS stars. The relation between observed flux and calibrated flux ($f_{\rm cal}^{N191}$) is as follows,

$$F_{\rm obs}^{N191} = \zeta_{\rm ANIR} (T_{\rm atm}^{{\rm PWV},N191})^X f_{\rm cal}^{N191} \Delta\lambda. \tag{A6}$$

We can derive a calibrated flux of continuum ($f_{\rm cal}^{c}$) by the interpolated flux of H and $K_{\rm s}$ broad-band filter ($f_{\rm cal}^{H-K_{\rm s}}$), which are not affected by the atmospheric absorption ($f_{\rm cal}^{c} \equiv f_{\rm cal}^{H-K_{\rm s}}$). The relation between intrinsic flux of continuum ($F_{\rm int}^{c}$) and calibrated flux is as follows,

$$F_{\rm int}^{c} = \zeta_{\rm ANIR} f_{\rm cal}^{c} \Delta\lambda \tag{A7}$$

$$= \zeta_{\rm ANIR} f_{\rm cal}^{H-K_{\rm s}} \Delta\lambda. \tag{A8}$$

Then, we can obtain the following equation by using (A5), (A6) and (A8),

$$F_{\rm int}^{l} = \frac{(T_{\rm atm}^{{\rm PWV},N191})^X}{T_{\rm line}} (f_{\rm cal}^{N191} - f_{\rm cal}^{H-K_{\rm s}}) \Delta\lambda. \tag{A9}$$